



# 1 A seasonal analysis of aerosol $\text{NO}_3^-$ sources and $\text{NO}_x$ oxidation 2 pathways in the Southern Ocean marine boundary layer

3 Jessica M. Burger<sup>1</sup>, Emily Joyce<sup>2</sup>, Meredith G. Hastings<sup>2</sup>, Kurt A. M. Spence<sup>1</sup>, Katye E.  
4 Altieri<sup>1</sup>

5 <sup>1</sup>Department of Oceanography, University of Cape Town, Rondebosch, 7701, South Africa

6 <sup>2</sup>Department of Earth, Environmental and Planetary Sciences and Institute at Brown for Environment and  
7 Society, Brown University, Providence, RI, 02906, USA.

8 Correspondence to: Jessica M. Burger (brgjes006@uct.ac.za)

9 **Abstract.** Nitrogen oxides, collectively referred to as  $\text{NO}_x$  ( $\text{NO} + \text{NO}_2$ ), are an important component of  
10 atmospheric chemistry involved in the production and destruction of various oxidants that contribute to the  
11 oxidative capacity of the troposphere. The primary sink for  $\text{NO}_x$  is atmospheric nitrate, which has an influence  
12 on climate and the biogeochemical cycling of reactive nitrogen.  $\text{NO}_x$  sources and  $\text{NO}_x$  to  $\text{NO}_3^-$  formation  
13 pathways remain poorly constrained in the remote marine boundary layer of the Southern Ocean (SO),  
14 particularly outside of the more frequently sampled summer months. This study presents seasonally resolved  
15 measurements of the isotopic composition ( $\delta^{15}\text{N}$ ,  $\delta^{18}\text{O}$  and  $\Delta^{17}\text{O}$ ) of atmospheric nitrate in coarse mode ( $> 1\mu\text{m}$ )  
16 aerosols, collected between South Africa and the sea ice edge in summer, winter and spring. Similar latitudinal  
17 trends in  $\delta^{15}\text{N}\text{-NO}_3^-$  were observed in summer and spring, suggesting similar  $\text{NO}_x$  sources. Based on  $\delta^{15}\text{N}\text{-NO}_3^-$ ,  
18 the primary  $\text{NO}_x$  sources were lightning, oceanic alkyl nitrates and snowpack emissions at the low, mid and high  
19 latitudes, respectively. Snowpack emissions associated with photolysis were derived from both the Antarctic  
20 snowpack as well as from snow on sea ice. A combination of natural  $\text{NO}_x$  sources, likely transported from the  
21 lower latitude Atlantic contribute to the background level  $\text{NO}_3^-$  observed in winter, with the potential for a  
22 stratospheric  $\text{NO}_x$  source evidenced by one sample of Antarctic origin. Low summertime  $\delta^{18}\text{O}\text{-NO}_3^-$  ( $< \sim 70\text{‰}$ )  
23 are consistent with daytime processes involving oxidation by OH dominating nitrate formation, while higher  
24 winter and springtime  $\delta^{18}\text{O}\text{-NO}_3^-$  ( $> \sim 60\text{‰}$ ) indicate an increased influence of  $\text{O}_3$  oxidation (i.e.,  $\text{N}_2\text{O}_5$ , DMS,  
25  $\text{BrO}$ ). Significant linear relationships between  $\delta^{18}\text{O}$  and  $\Delta^{17}\text{O}$  suggest isotopic mixing between  $\text{H}_2\text{O}_{(\text{v})}$  and  $\text{O}_3$  in  
26 winter, with the addition of a third endmember (atmospheric  $\text{O}_2$ ) becoming relevant in spring. The onset of  
27 sunlight in spring, coupled with large sea ice extent, can activate chlorine chemistry with the potential to  
28 increase peroxy radical concentrations, contributing to oxidant chemistry in the marine boundary layer.

## 29 1 Introduction

30 The atmosphere of the Southern Ocean is geographically remote from major anthropogenic influences.  
31 Although there is evidence of microplastics and at times long-range transport of anthropogenic pollution (Jacobi  
32 et al., 2000; Obbard 2018;), the Southern Ocean marine boundary layer (MBL) is one of the few regions  
33 dominated by natural sources, and as such at times it can serve as a proxy for the pre-industrial atmosphere. The  
34 pre-industrial atmosphere is used as a baseline for comparing the magnitude of anthropogenic impacts on  
35 climate (e.g., Haywood and Boucher, 2000; Hamilton et al., 2014; Schmale et al., 2019).

36 Nitrogen oxides ( $\text{NO}_x = \text{NO} + \text{NO}_2$ ) are an important part of biogeochemical cycling and influence the oxidative  
37 capacity of the troposphere as they are involved in the production and destruction of ozone and hydroxyl  
38 radicals (Lawrence and Crutzen, 1999; Finlayson-Pitts and Pitts, 2000). The primary sink for  $\text{NO}_x$  is



atmospheric nitrate ( $\text{NO}_3^-$ ), which impacts both air quality and climate by influencing particulate matter load and Earth's radiative heat budget (IPCC, 2013; (Park and Kim, 2005)).

The logistical difficulties of measurement campaigns to the remote Southern Ocean, particularly in winter, have resulted in a lack of observational data from this region including that of  $\text{NO}_x$  sources and sinks (Paton-Walsh et al., 2022). Consequently, the seasonality of  $\text{NO}_x$  cycling remains poorly constrained in the Southern Ocean MBL. Globally, fossil fuel combustion is the primary  $\text{NO}_x$  source (van der A et al., 2008), far exceeding natural emissions like biomass burning (Finlayson-Pitts and Pitts, 2000), soil processes (Davidson and Kinglerlee, 1997) and lightning (Schumann and Huntrieser, 2007). However, regional budgets of  $\text{NO}_x$  sources can have a variety of anthropogenic and natural contributors. In the summertime Southern Ocean MBL, natural  $\text{NO}_x$  sources are the primary contributors to atmospheric  $\text{NO}_3^-$  formation (Morin et al., 2009; Burger et al., 2022). Along the South African coastline, these natural  $\text{NO}_x$  sources include a combination of lightning, biomass burning and soil emissions (Morin et al., 2009). In coastal Antarctica, or near to the marginal ice zone,  $\text{NO}_x$  emitted from snow cover serves as the primary precursor to atmospheric  $\text{NO}_3^-$  (Savarino et al., 2007; Morin et al., 2009; Shi et al., 2021; Burger et al., 2022). Over the mid-latitude region of the Southern Ocean, sea surface emissions of a group of nitrogen gases referred to as alkyl nitrates ( $\text{RONO}_2$ ), have recently been proposed as a  $\text{NO}_x$  source leading to  $\text{NO}_3^-$  formation in the MBL (Fisher et al., 2018; Burger et al., 2022). During winter,  $\text{NO}_x$  sources to the Antarctic troposphere primarily include long-range transported peroxyacetyl nitrates (PAN) and stratospheric inputs (Savarino et al., 2007; Lee et al., 2014; Walters et al., 2019). To our knowledge, however, there are no observational data regarding  $\text{NO}_x$  sources from the Southern Ocean MBL during winter, and few observations in spring.

In addition to there being multiple  $\text{NO}_x$  sources across the Southern Ocean MBL, several different oxidation pathways can be responsible for  $\text{NO}_x$  to  $\text{NO}_3^-$  conversion, varying with chemistry and time of day (Savarino et al., 2007). On a global scale, NO is primarily oxidised to  $\text{NO}_2$  by ozone ( $\text{O}_3$ ), although over the open ocean oxidation by peroxy radicals ( $\text{HO}_2$  and  $\text{RO}_2$ ) can also occur (Alexander et al., 2020). During summer in the Southern Ocean MBL,  $\text{NO}_2$  is subsequently oxidised primarily by hydroxyl radicals (OH) to form  $\text{HNO}_3$ . In winter, under dark conditions, when the photolytic production of OH stops,  $\text{NO}_2$  is oxidised primarily by  $\text{O}_3$  to form nitrate radicals ( $\text{NO}_3$ ).  $\text{NO}_3$  can then react with  $\text{NO}_2$  to form dinitrogen pentoxide ( $\text{N}_2\text{O}_5$ ) followed by hydrolysis on a wet particle surface to form  $\text{HNO}_3$ . Alternatively,  $\text{HNO}_3$  can be formed by the reaction of  $\text{NO}_3$  with hydrocarbons (HC) (e.g., dimethylsulphide (DMS)). Lastly, in places with elevated halogen concentrations,  $\text{NO}_2$  can be oxidised by reactive halogens (e.g., bromine oxide ( $\text{BrO}$ )), to form  $\text{HNO}_3$ .

The nitrogen (N) and oxygen (O) isotopic composition of atmospheric  $\text{NO}_3^-$  provides information regarding  $\text{NO}_x$  sources and  $\text{NO}_3^-$  formation pathways (i.e., NO oxidation to  $\text{NO}_2$  and  $\text{NO}_2$  oxidation to  $\text{NO}_3^-$ ). This technique has been applied in polluted (Elliot et al., 2007; Zong et al., 2017), open ocean (Hastings et al., 2003; Altieri et al., 2013; Kamezaki et al., 2019; Burger et al., 2022) and polar environments (Walters et al., 2019). Stable isotope ratios are reported as the ratio of the heavy to light isotopologues of a sample relative to the constant isotopic ratio of a reference standard, using delta ( $\delta$ ) notation in units of “per mil” (‰) following Eq. (1):

$$\delta = \left( \left( R_{\text{sample}} / R_{\text{standard}} \right) - 1 \right) \times 1000 \quad (1)$$



77 where  $R$  represents the ratio of  $^{15}\text{N}/^{14}\text{N}$ ,  $^{18}\text{O}/^{16}\text{O}$  or  $^{17}\text{O}/^{16}\text{O}$  in the sample and in the reference standard,  
 78 respectively. The reference for O is Vienna Standard Mean Ocean Water (VSMOW) and for N is atmospheric  
 79  $\text{N}_2$  (Bolhke et al., 2003).

80 The N isotopic composition of atmospheric  $\text{NO}_3^-$  ( $\delta^{15}\text{N}\text{-NO}_3^-$ ) largely reflects the  $\delta^{15}\text{N}$  of different precursor  
 81  $\text{NO}_x$  emissions (e.g., Elliott et al., 2019 and references therein), but can be influenced by isotopic fractionation  
 82 during  $\text{NO}_x$  cycling and  $\text{NO}_x$  to  $\text{NO}_3^-$  conversion (Walters and Michalski 2015; Walters et al., 2016; Li et al.,  
 83 2021).  $\delta^{15}\text{N}\text{-NO}_3^-$  is therefore useful for constraining  $\text{NO}_x$  sources. For example, the  $\delta^{15}\text{N}$  of lightning  $\text{NO}_x$  is  
 84 approximately 0‰ (Hoering, 1957), and is distinct from the snowpack  $\text{NO}_x$  source, which typically has a very  
 85 low  $\delta^{15}\text{N}$  signature of  $\sim -48\text{‰}$  (Berhanu et al., 2014; Berhanu et al., 2015). Savarino et al., (2007) derived an  
 86 Antarctic stratospheric  $\text{NO}_x$  source signature of  $19 \pm 3\text{‰}$ . Additionally, Burger et al. (2022) estimated the  $\delta^{15}\text{N}$   
 87 signature of  $\text{NO}_x$  produced by surface ocean  $\text{RONO}_2$  emissions over the mid-latitude Southern Ocean to be  $\sim -$   
 88  $22\text{‰}$ .

89 The O isotopic composition of atmospheric  $\text{NO}_3^-$  ( $\delta^{18}\text{O}\text{-}$  and  $\Delta^{17}\text{O}\text{-NO}_3^-$ ) reflects the oxidants responsible for  
 90  $\text{NO}_3^-$  formation, as atmospheric oxidants have distinct O isotope signatures (Michalski et al., 2011).  $\delta^{18}\text{O}\text{-NO}_3^-$   
 91 and  $\Delta^{17}\text{O}\text{-NO}_3^-$  are thus useful for identifying pathways of  $\text{NO}_3^-$  production (Michalski et al., 2003; Hastings et  
 92 al., 2003; Alexander et al., 2020).  $\text{O}_3$  possesses a distinctively large  $^{17}\text{O}$  excess as a result of non-mass-  
 93 dependent isotope fractionation. This  $^{17}\text{O}$  excess is expressed as  $\Delta^{17}\text{O} = \delta^{17}\text{O} - 0.52 \times \delta^{18}\text{O}$  (Berhanu et al.,  
 94 2012). Non-mass dependent fractionation occurs in the troposphere and is related to UV photolysis breaking  
 95 oxygen molecules to form  $\text{O}_3$  (Ireland et al., 2020). As a result,  $\text{O}_3$  possesses a uniquely high terminal  $\Delta^{17}\text{O} =$   
 96  $39.2 \pm 2\text{‰}$  (Vicars and Savarino, 2014) that can be transferred to  $\text{NO}_3^-$  during oxidation reactions between  $\text{NO}_x$   
 97 and  $\text{O}_3$  (Thiemens 2006; Michalski and Bhattacharya, 2009).  $\Delta^{17}\text{O}\text{-NO}_3^-$  therefore serves as a proxy for the  
 98 influence of  $\text{O}_3$  during  $\text{NO}_3^-$  formation (Berhanu et al., 2012).

99  $\text{O}_3$  also has a uniquely high terminal  $\delta^{18}\text{O} = 126.3 \pm 11.9\text{‰}$  (Vicars and Savarino, 2014) compared to other  
 100 oxidants that have a  $\Delta^{17}\text{O}$  of 0‰ and much lower  $\delta^{18}\text{O}$  signatures (Michalski et al., 2003; Michalski et al.,  
 101 2011). For example, atmospheric  $\text{O}_2$  has a  $\delta^{18}\text{O}$  signature of 23.9‰ and the  $\delta^{18}\text{O}$  of OH and  $\text{H}_2\text{O}$  are negative  
 102 (Michalski et al., 2011). As such, a higher  $\delta^{18}\text{O}$  or  $\Delta^{17}\text{O}$  for atmospheric  $\text{NO}_3^-$  reflects the increased influence of  
 103  $\text{O}_3$  on  $\text{NO}_3^-$  formation, while a lower  $\delta^{18}\text{O}$  or  $\Delta^{17}\text{O}$  occurs when there is a lack of exchange of O atoms with  $\text{O}_3$   
 104 (Hastings et al., 2003; Fang et al., 2011; Altieri et al., 2013). Oxidation by peroxy radicals would also result in a  
 105 lower  $\delta^{18}\text{O}$  and  $\Delta^{17}\text{O}$  signature for atmospheric nitrate because the O atom in peroxy radicals derives from  
 106 atmosphere  $\text{O}_2$ .

107 Tropospheric oxidation chemistry has been well characterised using  $\Delta^{17}\text{O}$  at coastal (Savarino et al., 2007;  
 108 Ishino et al., 2017) and interior Antarctic sites (Frey et al., 2009; Savarino et al., 2016; Walters et al., 2019). A  
 109 distinct seasonal cycle in  $\Delta^{17}\text{O}\text{-NO}_3^-$  is generally observed whereby a higher relative contribution from  $\text{O}_3$   
 110 oxidation and/or stratospheric input occurs during winter, and more  $\text{HO}_x + \text{RO}_x$  oxidation occurs during  
 111 summer. The Atlantic Southern Ocean is less constrained in terms of oxidation chemistry, with growing  
 112 evidence that the atmospheric oxidant budget is poorly understood in unpolluted low- $\text{NO}_x$  environments (Beygi  
 113 et al., 2011).



This study presents the first seasonally resolved data set of coarse mode ( $> 1 \mu\text{m}$ ) atmospheric  $\text{NO}_3^-$  concentration and isotopic composition from the Atlantic Southern Ocean MBL. Using air mass back trajectories and observed aerosol  $\delta^{15}\text{N}-\text{NO}_3^-$ ,  $\delta^{18}\text{O}-\text{NO}_3^-$  and  $\Delta^{17}\text{O}-\text{NO}_3^-$  between Cape Town, South Africa and the marginal ice zone this work aims to identify how the main sources and formation pathways of  $\text{NO}_3^-$  vary over the remote Southern Ocean from winter through spring and summer.

## 2 Methods

### 2.1 Sample collection

Samples were collected on board the Research Vessel (R/V) *SA Agulhas II* during three voyages to and from the marginal ice zone in summer (7<sup>th</sup> to 21<sup>st</sup> December 2018 & 27<sup>th</sup> February to 15<sup>th</sup> March 2019), winter (19<sup>th</sup> July to 12<sup>th</sup> August 2019) and spring (13<sup>th</sup> October to 19<sup>th</sup> November 2019) (Fig. 1). The summer samples presented here are the same as those in Burger et al. (2022). The winter and spring samples were collected and analysed as in Burger et al. (2022), with any methodological modifications noted below. Briefly, all voyages departed from Cape Town (33.9° S, 18.4° E) and sailed southward along the Good Hope transect (0°E), until reaching Penguin Bukta (71.4° S, 2.5° W) in summer and the northern extent of the sea ice in winter (approximately 58.1° S) and spring (approximately 59.3° S). The ship then returned to Cape Town, sailing north via the Good Hope transect, with a deviation to South Georgia in the summer. In spring an additional ice edge transect was conducted during which the ship sailed from 0 to approximately 22° E and back, before returning to Cape Town.

Size-segregated aerosols were collected on the ninth floor above the bridge (approximately 20 m above sea level), using a high-volume air sampler (HV-AS; Tisch Environmental). Air was pumped at an average flow rate of  $1.3 \text{ m}^3 \text{ min}^{-1}$  through a five-stage cascade impactor (TE-235; Tisch Environmental), loaded with pre-combusted (400°C for 4 hours) glass fibre filters. Given that aerosol nitrate in the MBL is predominantly present in the coarse mode ( $> 1 \mu\text{m}$ ), only filter stages 1 through 4 were analysed. The aerodynamical diameter of particles captured by filter stages 1, 2, 3 and 4 are  $> 7 \mu\text{m}$ , 3 to 7  $\mu\text{m}$ , 1.5 to 3  $\mu\text{m}$  and 1 to 1.5  $\mu\text{m}$ , respectively.

A sector collector was used to restrict HV-AS activity to avoid contamination of the filters with ship stack emissions (Campbell Scientific Africa). The HV-AS only operated if the winds were blowing at an angle less than 120° or greater than 240° from the bow of the ship during winter, and less than 75° or greater than 190° from the bow of the ship during spring. These criteria were altered based on the dominant wind direction during each voyage to ensure sufficient sample collection while avoiding contamination. In addition to wind direction, the wind speed had to exceed  $0 \text{ m s}^{-1}$  for ten minutes for the HV-AS to begin sampling. Filters were removed from the cascade impactor inside a laminar flow cabinet (Air Science), placed in individual zip-sealed bags and stored at -20°C until analysis.

An attempt was made to ensure that there were at least 24 hours of in-sector sampling before removing filters from the cascade impactor, to ensure atmospheric  $\text{NO}_3^-$  concentrations were sufficient for isotope analysis (Sect. 2.3). However, this was not always possible as on occasion filters had to be removed early due to unusual ship manoeuvres that could have resulted in sample contamination by ship stack emissions if left unattended. Sampling duration ranged from 11 to 36 hours in winter and 7 to 41 hours in spring (Table S1).



During each voyage, a field blank was collected by fitting the cascade impactor with a set of filters and loading the HV-AS in the same manner that atmospheric samples were deployed. The cascade impactor was then immediately removed without turning on the HV-AS pump. The field blanks were removed from the cascade impactor and stored in the same manner as the atmospheric samples. All chemical analysis performed on samples was performed on the field blanks to assess any possible contamination during filter deployment or laboratory procedures.

## 2.2 Sample analysis

Filters were extracted using ultra-clean deionised water (DI; 18 MΩ) under a laminar flow cabinet (Air Science). The extraction ratio was approximately 30 cm<sup>2</sup> to 100 cm<sup>2</sup> of filter in 30 mL of DI. Extracts were immediately sonicated for one hour and then stored at 4°C for at least 12 hours. Thereafter, extracts were filtered (0.2 μm) using an acid washed syringe into clean 30 mL HDPE bottles and stored at -20°C until analysis (Burger et al., 2022).

[NO<sub>3</sub><sup>-</sup>] was determined using a Thermo Scientific Dionex Aquion Ion Chromatography (IC) system equipped with an autosampler. The anion IC contained an AG22 RFIC 4 x 50 mm guard column and AG22 RFIC 4 x 250 mm analytical column. A six-point standard curve was run on each day of analysis (Dionex Seven Anion-II Standard) and an R<sup>2</sup> value > 0.999 was required for sample analysis to proceed. Final [NO<sub>3</sub><sup>-</sup>] were corrected by subtracting the field blanks, which represented 32% and 59% of the [NO<sub>3</sub><sup>-</sup>] in winter and spring respectively. Where the field blank had a [NO<sub>3</sub><sup>-</sup>] greater than that of the sample, the sample [NO<sub>3</sub><sup>-</sup>] was assumed to be zero. Samples were measured for [NO<sub>3</sub><sup>-</sup>] only once to preserve sample volume for isotopic analysis (Sect. 2.3), motivated by the small difference between repeated sample measurements from the summertime dataset (SD<sub>p</sub> = 0.3 μmol L<sup>-1</sup>).

### 2.2.1 Isotopic analysis

The isotopic composition of atmospheric NO<sub>3</sub><sup>-</sup> (δ<sup>15</sup>N, δ<sup>18</sup>O, and Δ<sup>17</sup>O-NO<sub>3</sub><sup>-</sup>) was measured using the denitrifier method (Sigman et al., 2001; Casciotti et al., 2002; Kaiser et al., 2007). In brief, a natural strain of denitrifying bacteria, *Pseudomonas aureofaciens*, that lack the terminal nitrous oxide (N<sub>2</sub>O) reductase enzyme were used to convert aqueous NO<sub>3</sub><sup>-</sup> quantitatively to N<sub>2</sub>O gas. The product N<sub>2</sub>O was analyzed by Gas-Chromatograph IRMS (Thermo- Scientific Delta V Plus) for simultaneous isotopic determination of <sup>15</sup>N/<sup>14</sup>N and <sup>18</sup>O/<sup>16</sup>O (Sigman et al., 2001; Casciotti et al., 2002). The <sup>15</sup>N/<sup>14</sup>N of samples was corrected for the contribution of <sup>17</sup>O to the peak at mass 45 using Δ<sup>17</sup>O determined for each sample, with values ranging from 21.7‰ to 44.4‰. International reference materials (Table S2) IAEA-N3 and USGS34 were used to normalize isotopic values to air (δ<sup>15</sup>N), and IAEA-N3, USGS34 and USGS-35 were used to normalize to VSMOW (δ<sup>18</sup>O) scales. The pooled standard deviation of sample replicates and duplicates for δ<sup>15</sup>N was 0.19‰ (n = 16) and for δ<sup>18</sup>O was 0.27‰ (n = 16). The pooled standard deviations of sample references IAEA-N3, USGS-34, USGS-35 for δ<sup>15</sup>N and for δ<sup>18</sup>O are reported for each season in Table S3.

For winter and spring samples, Δ<sup>17</sup>O-NO<sub>3</sub><sup>-</sup> was characterized by using a separate 50 nmol aliquot to convert NO<sub>3</sub><sup>-</sup> to N<sub>2</sub>O, thermally decomposing the N<sub>2</sub>O to N<sub>2</sub> and O<sub>2</sub> in a gold furnace at 770°C and analyzing the isotopic composition of O<sub>2</sub> for determination of <sup>18</sup>O/<sup>16</sup>O and <sup>17</sup>O/<sup>16</sup>O (Kaiser et al., 2007; Fibiger et al., 2013).



187 The product  $O_2$  was referenced to USGS34 and USGS35, and a 50/50 mix of USGS34 and USGS35 was also  
188 quantified within runs serving as a quality control check. The pooled standard deviations for  $\Delta^{17}O$  were 0.84‰  
189 ( $n=21$ ), 0.90‰ ( $n=21$ ), and 0.61‰ ( $n=18$ ) for USGS34, USGS35, and the 50/50 mix, respectively. The pooled  
190 standard deviation of sample replicates and duplicates was 0.63‰ in winter and 0.31‰ in spring.

191

192 Seawater samples were collected in triplicate every two hours from the ships underway system (position at  
193 depth approximately 5 m) for the analysis of surface ocean nitrite concentrations ( $[NO_2^-]$ ).  $[NO_2^-]$  was analysed  
194 using the colorimetric method of Grasshof et al. (1983) using a Thermo Scientific Genesys 30 visible  
195 spectrophotometer (detection limit of  $0.05 \mu\text{mol L}^{-1}$ ).

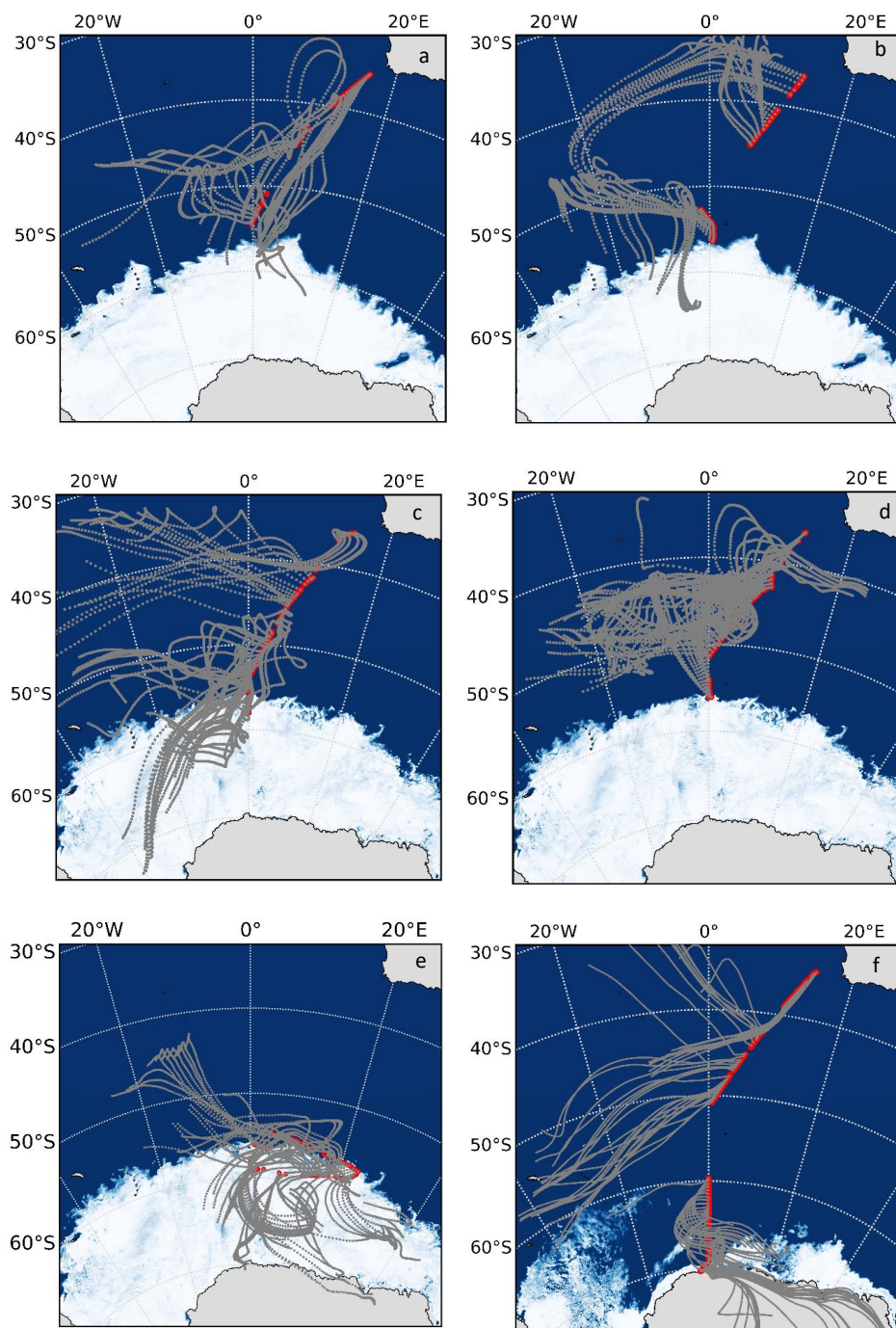
### 196 2.3 Air mass back trajectory analysis

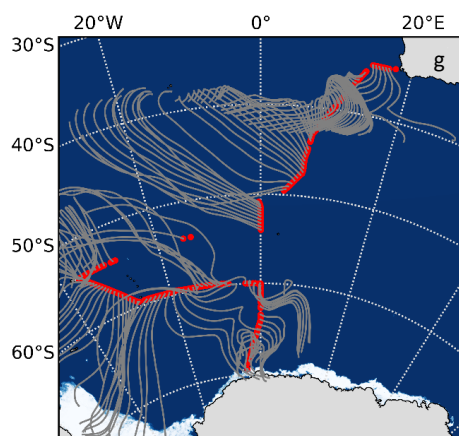
197 Airmass back trajectories (AMBTs) were computed for each hour in which the HV-AS was operational for at  
198 least 45 minutes of that hour. Given that the ship was moving, a different date, time and starting location was  
199 used to compute each AMBT. An altitude of 20 m was chosen to match the height of the HV-AS above sea level  
200 and 72-hour AMBTs were computed to account for the lifetime of  $NO_3^-$  in the atmosphere. All AMBTs were  
201 computed with NOAA's Hybrid Single-Particle Lagrangian Integrated Trajectory (HYSPLIT) model (Stein et  
202 al., 2015; Rolph et al., 2017), using NCEP Global Data Assimilation System (GDAS) output, which can be  
203 accessed at <http://www.arl.noaa.gov/ready/hysplit4.html> (NOAA Air Resources Laboratory, Silver spring,  
204 Maryland).

## 205 3 Results and Discussion

206 During all three seasons sampling was conducted across the Atlantic Southern Ocean. AMBTs indicate that no  
207 samples experienced any continental influence from South Africa (Fig 1), such that no direct anthropogenic  
208 emission sources are considered. 72-hour AMBTs confirm that the Atlantic sector of the Southern Ocean was a  
209 dominant source region for most samples collected throughout all seasons. Airmasses experienced very little  
210 interaction with sea ice in winter (Fig 1a & b), while extensive interaction with sea ice was experienced by  
211 airmasses sampled in spring, particularly at the high latitudes during the south bound leg (Fig 1c) and ice edge  
212 transect (Fig 1e). In summer, some high latitudes air masses traversed coastal Antarctica before being sampled,  
213 particularly on the south bound leg (Fig 1f), while some interaction with sea ice was also experienced by high  
214 latitude air masses on both legs (Fig 1f & g). As a result, air masses originated from a mixture of source regions  
215 ranging from the open ocean to sea ice to Antarctic continental ice. The remoteness of all the locations at which  
216 air masses originated from motivates the investigation of natural  $NO_x$  sources below.







218

219 Figure 1. 72-hour AMBTs computed for each hour of every filter deployment (grey lines) made in winter on  
 220 both the southbound (a) and northbound (b) voyages, in spring on the southbound voyage (c), ice edge transect  
 221 (d) and northbound voyage (e) and in summer on the southbound (f) and northbound (g) voyages. Red circles  
 222 indicate the ships cruise track during each filter deployment.

### 223 3.1 Seasonal variation in atmospheric $\text{NO}_3^-$ concentrations

224 In winter, atmospheric  $[\text{NO}_3^-]$  were very low across the Atlantic Southern Ocean ranging from below detection  
 225 to  $22.3 \text{ ng m}^{-3}$  (Fig. 2; blue diamonds). A single outlier exists with a relatively high  $[\text{NO}_3^-]$  equivalent to  $222.9$   
 226  $\text{ng m}^{-3}$  in winter, although it is comparable to summertime  $[\text{NO}_3^-]$  (Fig. 2; orange circles). In spring, atmospheric  
 227  $[\text{NO}_3^-]$  ranged from  $3.3 \text{ ng m}^{-3}$  to  $74.4 \text{ ng m}^{-3}$ , with one sample below detection limit. Higher  $[\text{NO}_3^-]$  were  
 228 observed at the lower latitudes and at the higher latitudes, while lower  $[\text{NO}_3^-]$  were observed in the mid-latitude  
 229 Atlantic Southern Ocean (Fig. 2; green squares). During summer atmospheric  $[\text{NO}_3^-]$  were higher than winter  
 230 and spring, ranging from  $19.9 \text{ ng m}^{-3}$  to  $264.0 \text{ ng m}^{-3}$ . In contrast to winter and spring, a distinct latitudinal trend  
 231 was observed in summer whereby the  $[\text{NO}_3^-]$  decreased with increasing latitude (Fig. 2; orange circles) (Burger  
 232 et al., 2022).



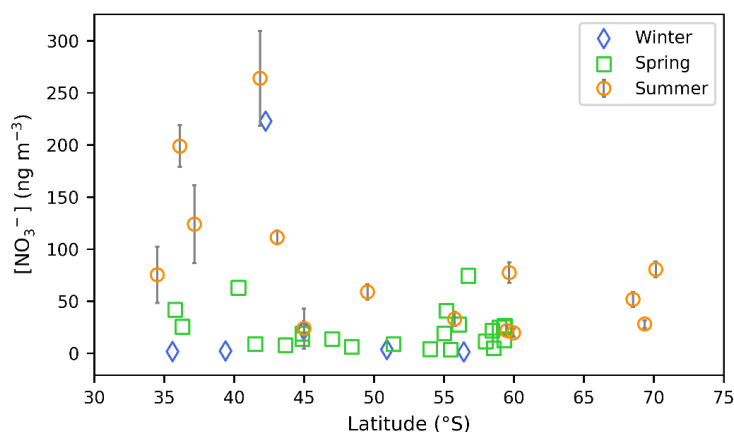


Figure 2. The average coarse mode ( $> 1 \mu\text{m}$ ) atmospheric nitrate concentration  $[\text{NO}_3^-]$  ( $\text{ng m}^{-3}$ ) as a function of latitude ( $^\circ \text{S}$ ). Winter, spring and summer are denoted by blue diamonds, green squares, and orange circles, respectively. For the summer data, where error bars ( $\pm 1 \text{ SD}$ ) are not visible, the standard deviation is smaller than the size of the marker.

The seasonal cycle in atmospheric  $[\text{NO}_3^-]$  that we observe, i.e., lowest concentrations in winter, higher in spring and highest in summer, is similar to previous observations for the region. Atmospheric  $[\text{NO}_3^-]$  ranging from tens of  $\text{ng m}^{-3}$  to approximately  $100 \text{ ng m}^{-3}$  have been observed for the Southern Ocean MBL during late spring (Morin et al., 2009; Shi et al., 2021) and observations from a coastal site at east Antarctica showed elevated  $[\text{NO}_3^-]$  ( $> \sim 40 \text{ ng m}^{-3}$ ) throughout late spring to early summer (Shi et al., 2022). Seasonal studies at coastal and inland Antarctic sites observed the lowest  $[\text{NO}_3^-]$  during winter (Savarino et al., 2007; Ishino et al., 2017; Walters et al., 2019).

The seasonality in atmospheric  $[\text{NO}_3^-]$  is largely driven by the seasonality in sunlight availability. Maximum atmospheric  $[\text{NO}_3^-]$  observed in late spring/early summer in coastal Antarctica were attributed to reactive N released from the post depositional processing/recycling of snow  $\text{NO}_3^-$  (Savarino et al., 2007). After  $\text{NO}_3^-$  is deposited to the snowpack, it can be photochemically reduced to  $\text{NO}_x$ , and (re)emitted to the overlying atmosphere (Jones et al., 2000; Jones et al., 2001). During winter, extended periods of darkness lead to reduced photochemical activity above the snow, resulting in background level  $[\text{NO}_3^-]$  (Lee et al., 2014). Over the open ocean, increased UV radiation in spring and summer compared to winter may lead to greater  $\text{NO}_3^-$  production from the photolytically derived oceanic  $\text{RONO}_2$  source (Fisher et al., 2018). Ground-based studies at various Antarctic sites demonstrate that UV radiation increases throughout spring and is highest in early summer (Lakkala et al., 2020; Li et al., 2020). This, in addition to greater lightning  $\text{NO}_x$  production during spring and summer at the lower southern latitudes ( $< 40 \text{ }^\circ \text{S}$ ) (Nesbitt et al., 2000) likely explain why higher  $[\text{NO}_3^-]$  are observed in spring and summer as compared to winter.

### 3.2 Seasonal variation in $\text{NO}_x$ sources

While  $[\text{NO}_3^-]$  provides valuable information regarding the seasonal and spatial variation in the quantity of tropospheric  $\text{NO}_3^-$  present, the N isotopic composition serves as a useful tool for identifying  $\text{NO}_x$  sources that



lead to aerosol  $\text{NO}_3^-$  formation. Here, we present and interpret the mass weighted coarse-mode average  $\delta^{15}\text{N}$ - $\text{NO}_3^-$ , computed for each filter deployment.

### 3.2.1 Evidence for stratospheric $\text{NO}_x$

There was one unusually high  $\delta^{15}\text{N}$ - $\text{NO}_3^-$  value equivalent to 16.6‰ for the first filter deployment of the southbound leg in winter. Despite an elevated  $\delta^{15}\text{N}$  signature, its  $[\text{NO}_3^-]$  was consistent with that of most wintertime samples. The  $\delta^{15}\text{N}$ - $\text{NO}_3^-$  of this wintertime sample is similar to the  $\delta^{15}\text{N}$  of stratospherically sourced  $\text{NO}_3^-$ , estimated to be  $19 \pm 3\text{‰}$  (Savarino et al., 2007). Stratospheric input is additionally supported by the air mass history of this sample, which indicates that air originated from as far south as the sea ice edge for the duration of the sample deployment (Fig. 1a). Coastal Antarctic studies suggest that the deposition of PSCs during winter results in stratospheric  $\text{NO}_3^-$  inputs to the Antarctic troposphere (Wagenbach et al., 1998; Savarino et al., 2007). Winter, when this sample was collected is the only time of year when Antarctic temperatures are expected to be cold enough ( $< 195\text{ K}$ ) for polar stratospheric cloud (PSC) formation (von Savigny et al., 2005; Wang et al., 2008).

Furthermore, this sample is unique in that it has a relatively high  $\delta^{18}\text{O}$ - $\text{NO}_3^-$  and  $\Delta^{17}\text{O}$ - $\text{NO}_3^-$ , 120.2‰ and 44.5‰, respectively. Tropospheric oxidation typically produces  $\Delta^{17}\text{O}$ - $\text{NO}_3^-$  values ranging from 17.3‰ to 42.7‰ (Morin et al., 2011; Ishino et al., 2017; Walters et al., 2019). Stratospheric sourced  $\Delta^{17}\text{O}$ - $\text{NO}_3^-$  is elevated in comparison to tropospheric  $\Delta^{17}\text{O}$ - $\text{NO}_3^-$  because stratospheric  $\text{O}_3$  has a greater isotope anomaly than tropospheric  $\text{O}_3$ , and/or dominance of the  $\text{N}_2\text{O}_5$  and  $\text{ClONO}_2$  pathways allow for greater transfer of the anomaly to  $\text{NO}_3^-$  via  $\text{O}_3$  (Savarino et al., 2007; McCabe et al., 2007). High  $\Delta^{17}\text{O}$ - $\text{NO}_3^-$  ( $> \sim 40\text{‰}$ ) observed in winter, are often attributed to contributions by stratospheric denitrification (Savarino et al., 2007; McCabe et al., 2007; Frey et al., 2009; Walters et al., 2019). The combination of elevated  $\Delta^{17}\text{O}$ - $\text{NO}_3^-$  and  $\delta^{15}\text{N}$ - $\text{NO}_3^-$  is consistent with a stratospheric  $\text{NO}_3^-$  source for this sample. Given the evidence that this sample likely does not reflect tropospheric oxidation chemistry, it is left out of the below analysis.

### 3.2.2 Transported $\text{NO}_x$

Previous studies have shown that tropospheric transport of  $\text{NO}_x$  from the mid to low latitudes contributes to the Antarctic  $\text{NO}_3^-$  budget in winter (Lee et al., 2014; Shi et al., 2018). However, transported  $\text{NO}_x$  results in minimal  $\text{NO}_3^-$ , regarded as background level concentrations (Lee et al., 2014), consistent with most of our winter observations (Fig. 2; blue diamonds). During winter,  $\delta^{15}\text{N}$ - $\text{NO}_3^-$  was relatively invariant across the Atlantic Southern Ocean (Fig. 3; blue diamonds) with an average of  $-3.4 \pm 2.1\text{‰}$  ( $n = 5$ ). This is consistent with a lack of snowpack  $\text{NO}_x$  emissions at the high latitudes during July/August due to weak or absent solar radiation (Shi et al., 2022). Furthermore, air mass back trajectory analyses indicate that sea ice had a very minor influence on the winter samples (Fig. 1a & b).

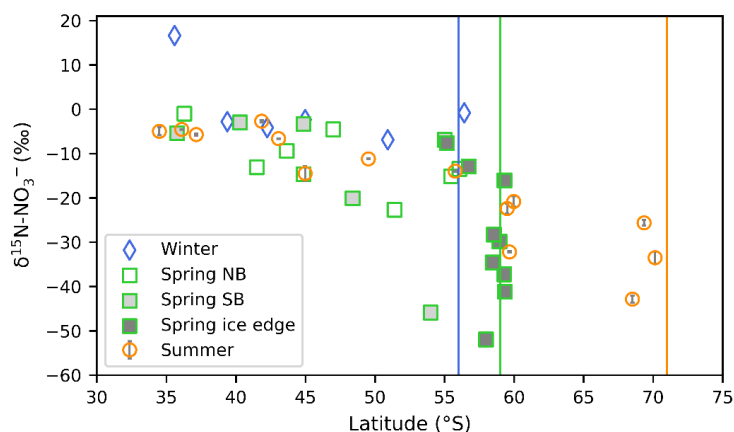


Figure 3. The weighted average  $\delta^{15}\text{N}$  of atmospheric nitrate ( $\delta^{15}\text{N-NO}_3^-$  (‰ vs.  $\text{N}_2$ )) as a function of latitude ( $^\circ\text{S}$ ). Winter, spring and summer are denoted by blue diamonds, green squares, and orange circles, respectively. For the summer data, where error bars ( $\pm 1$  SD) are not visible, the standard deviation is smaller than the size of the marker. Spring data are separated into northbound (NB), southbound (SB) and ice edge legs by clear, light grey and dark grey fills, respectively. Vertical lines indicate the approximate location of the sea ice edge in summer (orange), winter (blue) and spring (green), identified visually using satellite derived sea ice concentration obtained from passive microwave sensors AMSR2 (Advanced Microwave Scanning Radiometer 2; Spreen et al., 2008).

Albeit outside of the winter months, previous studies report an average  $\delta^{15}\text{N-NO}_3^-$  for the low latitude Atlantic Ocean (between  $45^\circ\text{S}$  and  $45^\circ\text{N}$ ) on the order of  $-3$  to  $-4$ ‰ (Baker et al., 2007; Morin et al., 2009), attributed to a combination of natural  $\text{NO}_x$  sources including lightning, biomass burning and soil emissions (Morin et al., 2009). This is also similar to the spring observations where higher values of  $\delta^{15}\text{N-NO}_3^-$  were observed at the lower latitudes ( $-3.2 \pm 1.8$ ‰;  $n = 3$ ). As such, the winter samples and low-latitude spring samples could be representative of a combination of natural  $\text{NO}_x$  sources emitted further north and transported to the mid-to-low latitude Atlantic Ocean.

Not all winter samples isotopically indicative of the transported background  $\text{NO}_x$  source had low  $[\text{NO}_3^-]$ . One unusually high  $[\text{NO}_3^-]$  value ( $222.9 \text{ ng m}^{-3}$ ) was observed in at the lower latitudes (Fig. 2; blue diamonds). Due to the similarity in isotopic composition among winter samples, we can assume that despite a higher  $[\text{NO}_3^-]$ , this sample also originated from a combination of natural  $\text{NO}_x$  sources transported from the lower latitudes. Furthermore a  $[\text{NO}_3^-]$  on the order of  $200 \text{ ng m}^{-3}$  is consistent with summertime  $[\text{NO}_3^-]$  observations (Fig 2; orange circles), when natural  $\text{NO}_x$  sources dominated (see section 3.2.3). Our results thus confirm that like in summer, natural  $\text{NO}_x$  sources can at times lead to relatively high  $[\text{NO}_3^-]$ , even in winter when background conditions are typically experienced.

In addition, the winter dataset presented here clearly highlights the utility of the isotopes in distinguishing  $\text{NO}_x$  sources. The initial winter sample had a low concentration indicative of the background conditions; however, the isotopic composition of the sample confirms that it originated from the stratosphere (see sect. 3.2.1). In



317 contrast, the anomalously high  $[\text{NO}_3^-]$  sample observed in winter was not consistent with minimal background  
318  $\text{NO}_x$  emissions, however its  $\delta^{15}\text{N}$  confirmed that this was in fact the most likely source.

### 319 3.2.3 Snowpack photolysis and oceanic $\text{NO}_x$ sources

320 Springtime  $\delta^{15}\text{N-NO}_3^-$  ranged from -52.0‰ to -1.1‰ and samples with the lowest  $\delta^{15}\text{N-NO}_3^-$  were observed at  
321 the high latitudes (Fig. 3; green squares). The range in  $\delta^{15}\text{N-NO}_3^-$  observed for spring is consistent with late  
322 spring/early summer (November to December) observations from the Indian Ocean sector of the Southern  
323 Ocean (Shi et al., 2021) and summer (December and March) observations from the Atlantic sector (Burger et al.,  
324 2022). Given the similarity in  $\delta^{15}\text{N-NO}_3^-$  between spring and summer we expect the dominant  $\text{NO}_x$  sources to be  
325 the same.

326 During spring, air mass back trajectories indicate substantial sea ice influence at the high latitudes during the  
327 southbound leg and during the ice edge transect (Fig. 4a & c). There is a large isotope effect associated with  
328 snow  $\text{NO}_3^-$  photolysis during summer in the Antarctic (Berhanu et al., 2014, 2015), resulting in the emission of  
329 low  $\delta^{15}\text{N-NO}_x$  ( $\sim -48\text{‰}$ ) to the overlying atmosphere (Savarino et al., 2007; Morin et al., 2009; Shi et al., 2018;  
330 Walters et al., 2019). The low  $\delta^{15}\text{N-NO}_3^-$  samples from the high latitudes (minimum -52.0‰) are clearly  
331 influenced by sea ice (Fig. 3, Fig. 4a & c), but the air masses do not cross the Antarctic continent. This suggests  
332 that the low  $\delta^{15}\text{N-NO}_x$  likely comes from snow nitrate photolysis from the snow on sea ice. We conclude that  
333  $\text{NO}_3^-$  photolysis from snow on sea ice can explain the relatively low  $\delta^{15}\text{N-NO}_3^-$  observed in samples collected at  
334 the high latitudes on the spring southbound leg and during the ice edge transect (Fig. 3 grey filled squares).

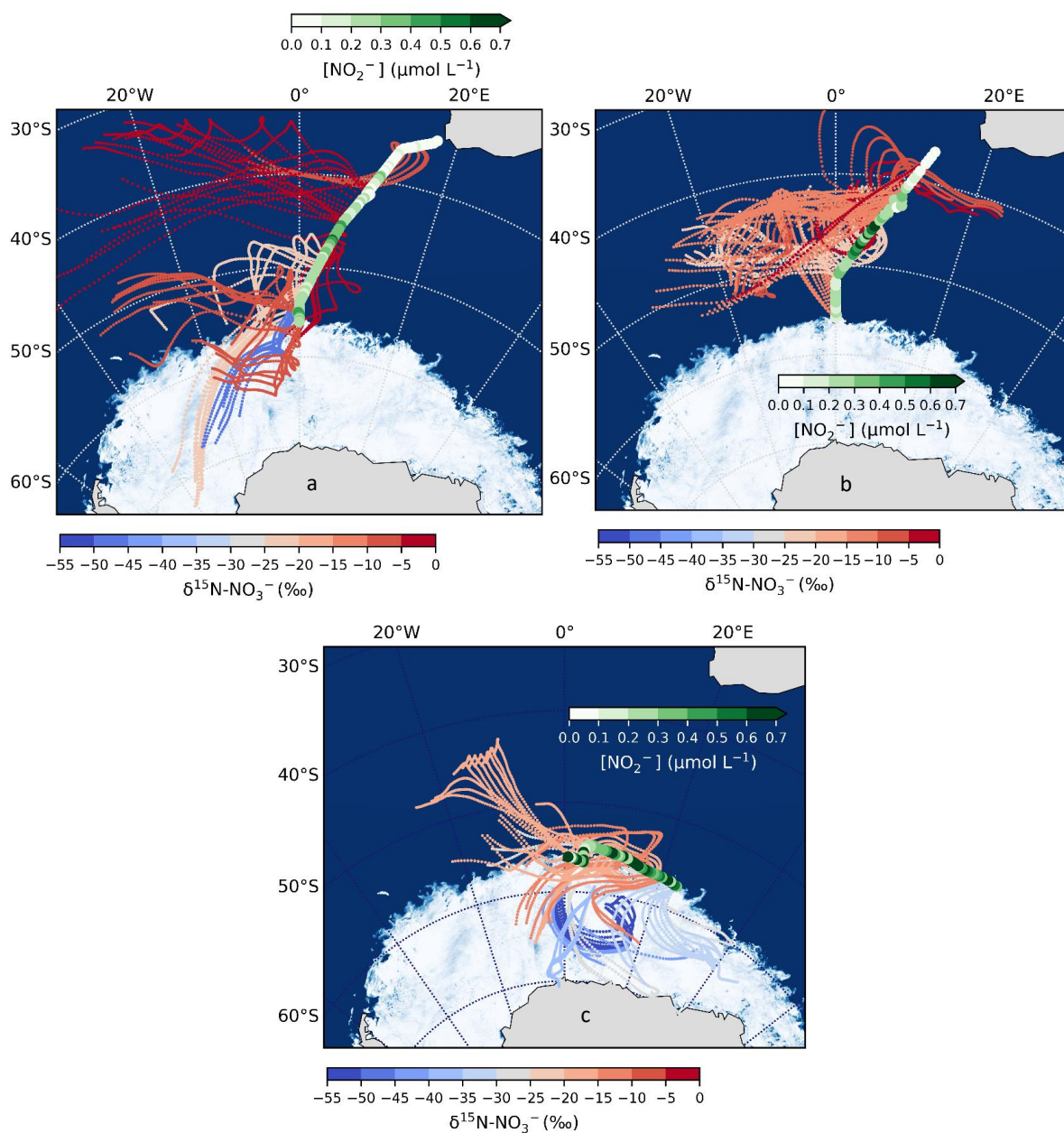


Figure 4. 72-hour AMBTs computed for each hour of the spring cruise during the southbound leg (a), the northbound leg (b) and the ice edge transect (c), when the HV-AS was running for more than 45 min of the hour. AMBTs are colour coded by the weighted average  $\delta^{15}\text{N-NO}_3^-$ , represented by the blue to red colour bar. Overlaid are the surface ocean nitrite concentrations ( $[\text{NO}_2^-]$ ), represented by the green colour bar. The white area represents the location of the sea ice determined using satellite-derived sea ice concentration data obtained



340 from the passive microwave sensors ASMR2 (Advanced Microwave Scanning Radiometer2; Spreen et al.,  
 341 2008).

342 Higher  $\delta^{15}\text{N-NO}_3^-$  values (-22.7 to -1.0‰) were observed during spring for samples with air mass histories that  
 343 indicate no contact with sea ice (i.e., the northbound leg; Fig. 3 open squares; Fig. 4b), suggesting limited  
 344 influence from snowpack  $\text{NO}_x$  emissions. These samples originated from over the mid-latitude region of the  
 345 Southern Ocean where detectable sea surface nitrite was present (Fig. 4b).  $\text{NO}$  derived from seawater nitrite is  
 346 thought to limit  $\text{RONO}_2$  production such that non-zero nitrite concentrations are required for  $\text{RONO}_2$  production  
 347 to occur in seawater (Dahl & Saltzman 2008; Dahl et al., 2012). Oceanic  $\text{RONO}_2$  has recently been proposed as  
 348 an important  $\text{NO}_3^-$  source to the region in summer (Fisher et al., 2018; Burger et al., 2022), however limited co-  
 349 occurring ocean atmosphere measurements are available to constrain the seasonality of the  $\text{RONO}_2$  source.  
 350 While  $\delta^{15}\text{N-RONO}_2$  has yet to be directly quantified, it was recently estimated to have an average  $\delta^{15}\text{N}$  signature  
 351 of  $\sim -22\text{‰}$  in the summertime Southern Ocean (Burger et al., 2022) and  $-27.8\text{‰}$  in the eastern equatorial Pacific  
 352 (Joyce et al., 2022). Consistent with this relatively isotopically light oceanic  $\text{RONO}_2$  source are observations of  
 353 relatively low aerosol  $\delta^{15}\text{N-NO}_3^-$  from the mid-latitude Southern Ocean (Burger et al., 2022) and eastern  
 354 equatorial Pacific (Kamezaki et al., 2019; Joyce et al., 2022), on the order of  $-15$  to  $-7\text{‰}$ .

355 Trends in  $\delta^{15}\text{N-NO}_3^-$  by air mass origin were most evident in the ice edge transect during which lower (higher)  
 356  $\delta^{15}\text{N-NO}_3^-$  values were observed for samples with greater sea ice (oceanic) influence (Fig. 4c). The photolysis  
 357 imprint on the  $\text{NO}_3^-$  stable isotope signal in the marine boundary layer above the sea ice is clearly observed and  
 358 speaks to the importance of snow-covered sea ice as a  $\text{NO}_x$  source in the region during spring as well as  
 359 summer. The increased importance of oceanic  $\text{RONO}_2$  emissions as air mass origin migrates from sea ice  
 360 covered to open ocean zones is also evidenced by the decrease in  $\delta^{15}\text{N-NO}_3^-$  observed for air mass originating  
 361 predominantly from over the ocean (Fig. 4c).

362 Isotopically, there is little evidence of  $\text{RONO}_2$  emissions contributing to aerosol  $\text{NO}_3^-$  in the winter samples.  
 363 Reduced levels of UV radiation and minimal daylight hours (Fig. S1) in winter likely hinders the contribution of  
 364 the oceanic  $\text{NO}_x$  source to  $\text{NO}_3^-$  loading compared to spring/summer, despite detectable sea surface nitrite  
 365 concentrations in winter (Fig. S2). Additionally, photolysis in spring/summer serves to produce  $\text{OH}$  which is the  
 366 primary oxidant for conversion of  $\text{RONO}_2$ -derived  $\text{NO}_x$  in the MBL (Fisher et al., 2018).

367 Some studies suggest that the photolysis of particulate  $\text{NO}_3^-$  ( $\text{p-NO}_3^-$ ) associated with sea-salt aerosols in the  
 368 MBL can serve as an important  $\text{NO}_x$  source (Zhou et al., 2003; Ye et al., 2016; Reed et al., 2017). However, the  
 369 importance of this  $\text{NO}_x$  formation pathway remains unclear, with large variability in reported rates between  
 370 studies (Ye et al., 2016; Reed et al., 2017; Kasibhatla et al., 2018; Romer et al., 2018). To our knowledge, there  
 371 are no observations of  $\text{p-NO}_3^-$  photolysis from the Southern Ocean MBL, and the implications of this process on  
 372 the isotopic composition of  $\text{NO}_3^-$  in the MBL have yet to be assessed. We know that  $\text{NO}_3^-$  photolysis in snow is  
 373 associated with a large fractionation, leading to the emission of isotopically light  $\text{NO}_x$  while the remaining  $\text{NO}_3^-$   
 374 pool becomes enriched in  $^{15}\text{N}$  (eg., Shi et al., 2018). Thus, if the  $\text{p-NO}_3^-$  we measured was affected by photolysis  
 375 we would have expected to observe much higher or even positive values of  $\delta^{15}\text{N-NO}_3^-$  during spring and  
 376 summer. Another scenario is that the  $\text{p-NO}_3^-$  we measured resulted from the oxidation of  $\text{NO}_x$  released by prior  
 377  $\text{p-NO}_3^-$  photolysis. In this case, we would have expected to observe much lower  $\delta^{15}\text{N-NO}_3^-$  values over the open





ocean, on par with those observed over the ice. Since neither of the above scenarios matches the observations, we discount the potential influence of aerosol  $\text{NO}_3^-$  photolysis as a significant  $\text{NO}_x$  source to the region during our study.

### 3.3 Seasonal variation in oxidation

As mentioned in Sect. 1.1, the oxidation of NO and  $\text{NO}_2$  can be determined using the oxygen isotopic composition of aerosol  $\text{NO}_3^-$ . Here, we present and interpret the mass weighted coarse-mode average  $\delta^{18}\text{O}-\text{NO}_3^-$  and  $\Delta^{17}\text{O}-\text{NO}_3^-$ , computed for each filter deployment.

During NO and  $\text{NO}_2$  oxidation, the oxygen atoms of the responsible oxidants are incorporated into the  $\text{NO}_3^-$  product. The transferrable terminal oxygen atom of  $\text{O}_3$  possesses an elevated  $\Delta^{17}\text{O}-\text{NO}_3^- (\text{O}_{3\text{term}})$  and  $\delta^{18}\text{O}(\text{O}_{3\text{term}})$  ( $39.3 \pm 2\%$  and  $126.3 \pm 11.9\%$ , respectively) (Vicars & Savarino, 2014), compared to other oxidants (e.g., OH and peroxy radicals ( $\text{RO}_2/\text{HO}_2$ )) which possess a  $\Delta^{17}\text{O}-\text{NO}_3^- \approx 0\%$  (Michalski et al., 2011). The  $\delta^{18}\text{O}$  of OH is negative while the  $\delta^{18}\text{O}$  of  $\text{RO}_2/\text{HO}_2$  stems from that of atmospheric  $\text{O}_2$  which is also low ( $23.9\%$ ; Barkan and Luz 2005). These differences allow us to quantitatively assess NO and  $\text{NO}_2$  oxidation chemistry involving contributions by various oxidants, as prior work suggests that oxidant  $\delta^{18}\text{O}$  values are directly represented in the  $\text{NO}_3^-$ .

The relatively low  $\delta^{18}\text{O}-\text{NO}_3^-$  values observed in summer ( $< 70\%$ ; Fig. 5) are consistent with  $\text{NO}_2$  oxidation via OH (Burger et al., 2022). During summer, unusually low  $\delta^{18}\text{O}-\text{NO}_3^-$  values were also observed equating to less than the minimum expected for the OH oxidation pathway ( $< \sim 46\%$ ; Burger et al., 2022). This was attributed to an increased contribution by  $\text{HO}_2/\text{RO}_2$  during NO oxidation to  $\text{NO}_2$  (as opposed to  $\text{O}_3$ ) which would decrease the  $\delta^{18}\text{O}$  of the product  $\text{NO}_3^-$ . Increased abundance of  $\text{RO}_2$  in the MBL was attributed to  $\text{RONO}_2$  photolysis, hypothesized to occur over the mid latitude Southern Ocean (Fisher et al., 2018; Burger et al., 2022), and/or the presence of sea ice, which can lead to enhanced peroxy radical production (Brough et al., 2019).

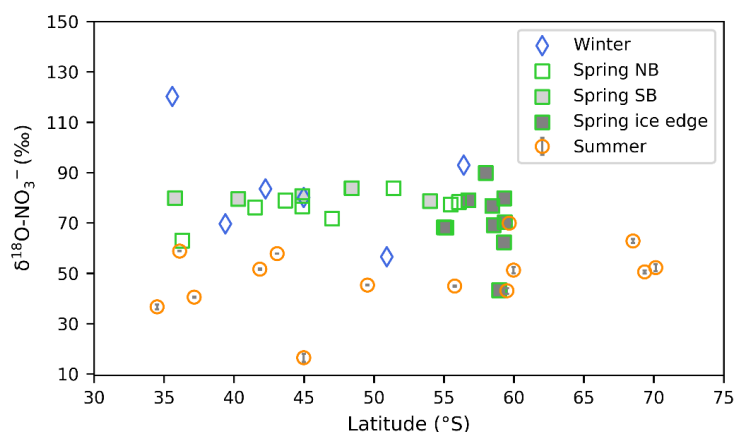


Figure 5. The weighted average  $\delta^{18}\text{O}$  of atmospheric nitrate ( $\delta^{18}\text{O}-\text{NO}_3^-$  (‰ vs. VSMOW)) as a function of latitude ( $^\circ\text{S}$ ). Winter, spring and summer are denoted by blue diamonds, green squares, and orange circles, respectively. Spring data are separated into northbound (NB), southbound (SB) and ice edge legs by clear, light



grey and dark grey fills, respectively. For the summer data, where error bars ( $\pm 1$  SD) are not visible, the standard deviation is smaller than the size of the marker.

Interestingly, despite  $\text{NO}_x$  sources being the same in spring and summer (sect. 3.2), the  $\delta^{18}\text{O}\text{-NO}_3^-$  data suggest that the  $\text{NO}_3^-$  formation pathways differ (Fig. 5). Higher average  $\delta^{18}\text{O}\text{-NO}_3^-$  values were observed in spring compared to summer (Fig. 5). Indeed, the oxygen isotopic composition of  $\text{NO}_3^-$  in winter and spring were comparable as indicated by both  $\delta^{18}\text{O}$  (Fig. 5) and  $\Delta^{17}\text{O}$  (Fig. S3). The  $\delta^{18}\text{O}\text{-NO}_3^-$  ranged from 56.5‰ to 92.9‰ in winter (Fig. 5; blue diamonds) and from 62.3‰ to 89.8‰ in spring (Fig. 5; green squares). The  $\Delta^{17}\text{O}\text{-NO}_3^-$  ranged from 22.3‰ to 35‰ in winter (Fig. S3; blue diamonds) and from 18.7‰ to 33.6‰ in spring (Fig. S3; green squares). Interestingly, there is more variability in the  $\delta^{18}\text{O}$  and  $\Delta^{17}\text{O}$  for the ice edge transect (Fig. 5 & S3; dark shaded squares) than the north and southbound transects. The overlap in  $\delta^{18}\text{O}$  and  $\Delta^{17}\text{O}$  in winter and spring suggest that similar pathways lead to  $\text{NO}_3^-$  formation in both seasons.

A significant linear relationship was observed between  $\delta^{18}\text{O}\text{-NO}_3^-$  and  $\Delta^{17}\text{O}\text{-NO}_3^-$  in both winter and spring (Fig. S4). This suggests isotopic mixing between two major oxidants (e.g., Fibiger et al., 2013; Shi et al., 2021). As such, the highest end-member is representative of tropospheric  $\text{O}_3$ , with a  $\delta^{18}\text{O}$  of  $\sim 114$  to  $138$ ‰ and a  $\Delta^{17}\text{O}$  of  $\sim 39$ ‰. There are multiple options for the second oxidant with a  $\Delta^{17}\text{O} = 0$ ‰, i.e., water vapour ( $\text{H}_2\text{O}_{(\text{v})}$ ), OH, and  $\text{O}_2$ . Here, we use the  $\delta^{18}\text{O}\text{-H}_2\text{O}_{(\text{v})}$  from the average of observations along a similar cruise transect from the Indian sector of the Southern Ocean (Dar et al., 2020). The average  $\delta^{18}\text{O}\text{-H}_2\text{O}_{(\text{v})}$  determined between  $\sim 33^\circ$  S and  $\sim 60^\circ$  S ( $-13.9 \pm 1.4$ ‰) was used for the winter samples given that AMBTs indicate that most air masses originated within this latitudinal band, where there is minimal variation in  $\delta^{18}\text{O}\text{-H}_2\text{O}_{(\text{v})}$  (Dar et al., 2020). In spring, the zone of air mass origin for our samples extends further south to  $\sim 70^\circ$  S. As shown by Dar et al. (2020),  $\delta^{18}\text{O}\text{-H}_2\text{O}_{(\text{v})}$  declines significantly between  $\sim 60^\circ$  S and  $\sim 70^\circ$  S. To account for this lowering in  $\delta^{18}\text{O}\text{-H}_2\text{O}_{(\text{v})}$  which could influence higher latitude samples, an additional  $\text{H}_2\text{O}_{(\text{v})}$  end member equivalent to the minimum observed by Dar et al., 2020 ( $-27.5$ ‰) was included for spring. The  $\delta^{18}\text{O}\text{-OH}$  was calculated from the equilibrium fractionation between OH and  $\text{H}_2\text{O}_{(\text{v})}$  (Michalski et al., 2011) using the observed atmospheric temperature range for winter and spring. The  $\delta^{18}\text{O}\text{-OH}$  determined for winter ranges from  $-56.2$  to  $-49.5$ ‰ (average =  $-52.8$ ‰) and for spring ranges from  $-54.5$  to  $-50.5$ ‰ (average =  $-52.5$ ‰). Therefore, a value of  $-52$ ‰ was used for both seasons. The atmospheric  $\delta^{18}\text{O}\text{-O}_2$  is well-constrained at  $23.9$ ‰ (Barkan and Luz 2005). Mixing lines for the three oxidant pairs ( $\text{OH}/\text{O}_3$ ,  $\text{H}_2\text{O}_{(\text{v})}/\text{O}_3$  and  $\text{O}_2/\text{O}_3$ ) are indicated by the grey, orange and red lines, respectively in Figure 6.

To determine the lower endmember in each season, i.e., the second major oxidant in addition to ozone, a straight line was fitted to the data in  $\delta^{18}\text{O}\text{-}\Delta^{17}\text{O}$  space and the x-intercept at a  $\Delta^{17}\text{O} = 0$ ‰ was determined. The x-intercept in winter is  $\sim 16$ ‰. During winter, the linear relationship observed (Fig. 6a) is similar to what has been seen in the Indian Ocean MBL and at coastal east Antarctica, where the x intercept was  $-11 \pm 8$ ‰ (Shi et al., 2021) and  $-15 \pm 6$ ‰ (Shi et al., 2022), respectively. The oxygen isotopic composition of the lower end member in our winter data is most similar to that of  $\text{H}_2\text{O}_{(\text{v})}$ . This is consistent with the average  $\delta^{18}\text{O}\text{-H}_2\text{O}_{(\text{v})}$  ( $= -13.6 \pm 1.5$ ‰) observed between approximately  $33^\circ$  S and  $60^\circ$  S (Dar et al., 2020). Therefore, a mixing line between  $\text{H}_2\text{O}_{(\text{v})}$  and  $\text{O}_3$  is the best fit to the winter observations (Fig. 6a; solid orange line).

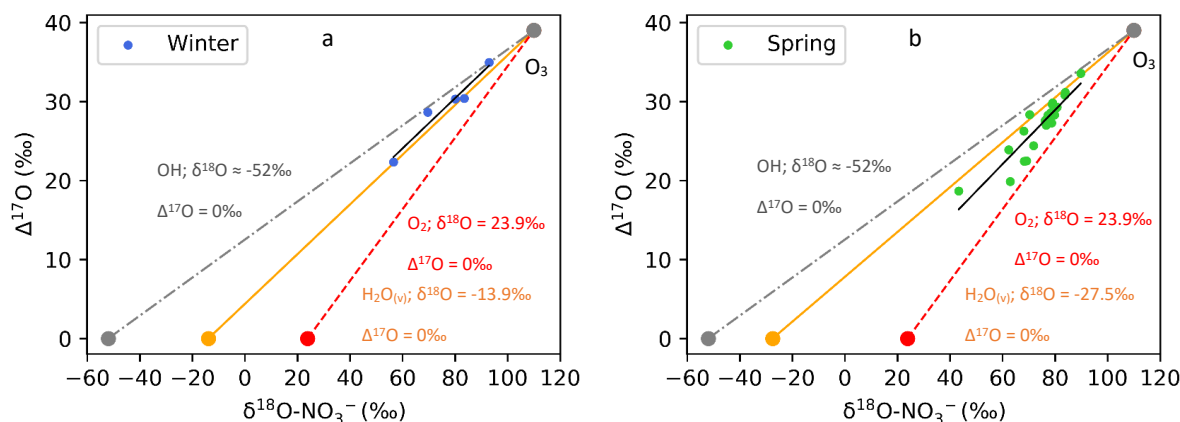


Figure 6. Winter and spring  $\delta^{18}\text{O}\text{-NO}_3^-$  vs.  $\Delta^{17}\text{O}\text{-NO}_3^-$  are plotted in panels (a) and (b), respectively. A straight line (black) is fitted to the data in each panel. In both panels the grey line represents the OH/ $\text{O}_3$  mixing line, the orange line represents the  $\text{H}_2\text{O}_{(\text{v})}$ / $\text{O}_3$  mixing line and the red line represents the  $\text{O}_2$ / $\text{O}_3$  mixing line.

By contrast, observations made in spring are best represented by mixing between 3 major oxidants:  $\text{H}_2\text{O}_{(\text{v})}$ ,  $\text{O}_3$  and  $\text{O}_2$ . The x-intercept in spring is  $\sim 4\text{‰}$ , making it more difficult to identify one low  $\delta^{18}\text{O}$  end member. The oxidant with the closest oxygen isotope composition is again  $\text{H}_2\text{O}_{(\text{v})}$ , however the x-intercept is greater in spring compared to winter, suggesting that the lower end member has a higher  $\delta^{18}\text{O}$ .  $\text{H}_2\text{O}_{(\text{v})}$  data from the region suggest that we would not expect to see a  $\delta^{18}\text{O} > -10\text{‰}$ , therefore an increase in  $\text{H}_2\text{O}_{(\text{v})}$   $\delta^{18}\text{O}$  from winter to spring can be ruled out. A more likely explanation is that the springtime lower endmember consists of some combination of  $\text{H}_2\text{O}_{(\text{v})}$  and an additional higher  $\delta^{18}\text{O}$  oxidant that is less abundant in winter. The higher  $\delta^{18}\text{O}$  oxidant is likely atmospheric  $\text{O}_2$  ( $\delta^{18}\text{O} = 23.9\text{‰}$ ,  $\Delta^{17}\text{O} = 0\text{‰}$  vs VSMOW; Barkan and Luz, 2005). This is consistent with the spread in the springtime observations, which are bound by the decreased  $\text{H}_2\text{O}_{(\text{v})}$ / $\text{O}_3$  mixing line to accommodate the influence of lower  $\delta^{18}\text{O}\text{-H}_2\text{O}_{(\text{v})}$  at the high latitudes (Fig. 6b; orange line), and the atmospheric  $\text{O}_2$ / $\text{O}_3$  mixing line (Fig. 6b; red line).

The influence of atmospheric  $\text{O}_2$  during spring likely results from the increased role for  $\text{RO}_2$  (and/or  $\text{HO}_2$ ) in  $\text{NO}_x$  cycling. This may be linked to increased  $\text{RO}_2$  production over the mid-latitude Southern Ocean, derived from  $\text{RONO}_2$  photolysis in the MBL (Burger et al., 2022). There is also evidence that sea ice can lead to enhanced peroxy radical production (Brough et al., 2019), resulting in the potential for increased  $\text{RO}_2$  and  $\text{HO}_2$  concentrations to be observed in air masses that traverse the sea ice zone before being sampled.  $\delta^{18}\text{O}\text{-NO}_3^-$  is greater in winter and spring compared to summer (Fig. 5), highlighting the increased control of  $\text{O}_3$  on the oxygen isotopic composition of  $\text{NO}_3^-$  in winter and spring. Consistent with increased  $\text{O}_3$  influence are seasonally resolved observations of  $\text{O}_3$  concentration ( $[\text{O}_3]$ ) at coastal Antarctica (Ishino et al., 2017; Shi et al, 2022) and Cape Grim, Tasmania (Derwent et al., 2016), the latter being more representative of the MBL. In all cases, maximum  $[\text{O}_3]$  are observed in winter, and minimum  $[\text{O}_3]$  are observed throughout summer. In spring,  $[\text{O}_3]$  concentrations are noticeably reduced compared to the winter, but slightly elevated compared to summer.



#### 466 4 Conclusions

467 Seasonally resolved observations of atmospheric  $\text{NO}_3^-$  across the Atlantic Southern Ocean MBL suggest that  
468 natural  $\text{NO}_x$  sources dominate throughout the year. Similar  $\text{NO}_3^-$  sources are available to the MBL in both spring  
469 and summer, highlighting the importance of oceanic  $\text{RONO}_2$  emissions in seasons other than the more  
470 frequently sampled summer months in the Southern Ocean. Although further research is required to improve our  
471 mechanistic and isotopic understanding of oceanic  $\text{RONO}_2$  formation, fluxes and conversion to aerosol  $\text{NO}_3^-$ ,  
472 this work contributes to our growing understanding of how the surface ocean influences the atmospheric  
473 reactive N cycle and oxidation chemistry of the MBL (Altieri et al., 2021; Burger et al., 2022; Joyce et al.,  
474 2022).

475 Furthermore, the large sea ice extent characteristic of spring highlights the importance of snow-covered sea ice  
476 as a  $\text{NO}_x$  source, in addition to the well documented summer source from snow covered continental ice (Jones et  
477 al., 2001; Walters et al., 2019; Winton et al., 2020). The presence of sea ice may also play a role in the  
478 formation of peroxy radicals through its influence on chlorine chemistry when sunlight is available (Brough et  
479 al., 2019). Peroxy radicals ( $\text{RO}_2$ ),  $\text{H}_2\text{O}_{(\text{v})}$  and  $\text{O}_3$  serve as the dominant atmospheric oxidants during spring,  
480 responsible for aerosol  $\text{NO}_3^-$  formation. In contrast, a lack of sunlight and sea ice influence is experienced  
481 during winter, and mixing between two end-members,  $\text{H}_2\text{O}_{(\text{v})}$  and  $\text{O}_3$ , best explain the oxygen isotopic  
482 composition of the  $\text{NO}_3^-$  that is formed. Similar to coastal Antarctic sites, reduced daylight hours and/or  
483 increased  $\text{O}_3$  abundance in the winter and spring MBL lead to greater  $\text{O}_3$  influence on  $\text{NO}_3^-$  formation, compared  
484 to the summer when OH oxidation chemistry dominates.

485 Winter is characterised by very low  $[\text{NO}_3^-]$  concentrations with  $\delta^{15}\text{N}$  signatures that reflect background  
486 conditions similar to that of the low latitude Atlantic Ocean (Morin et al., 2009). Interestingly, despite being  
487 collected off the coast of South Africa, the N and O isotopic composition of  $\text{NO}_3^-$  measured for the first  
488 wintertime sample reflects a stratospheric  $\text{NO}_x$  source signal. This is also supported by AMBTs that originate  
489 near Antarctica, where stratospheric denitrification is reported to occur (Savarino et al., 2007).

490 Our observations highlight the utility of the N isotopes in distinguishing between the various natural  $\text{NO}_x$   
491 sources that result in  $\text{NO}_3^-$  formation in the MBL of the Atlantic Southern Ocean, especially in the less  
492 frequently sampled seasons of winter and spring. Furthermore, the O isotopes serve as a useful tool for  
493 constraining formation pathways of aerosol  $\text{NO}_3^-$  seasonally, especially in the Atlantic Southern Ocean where  
494 oxidation chemistry is poorly constrained (Beygi et al., 2011). The contribution of sea ice to oxidant production  
495 when sunlight returns in spring is also highlighted by the O isotopes. As such, these data may be useful to  
496 modelling efforts attempting to characterise N cycling between the surface ocean and lower atmosphere, and  
497 may help improve atmospheric oxidant budgets that are less understood in unpolluted low- $\text{NO}_x$  environments.

498 **Author contributions.** KEA designed the study and sampling campaign, acquired funding and supervised the  
499 research. KEA and MGH provided financial and laboratory resources and assisted in data validation. EJ  
500 performed laboratory analysis of samples at Brown University. KAMS and JMB conducted the sampling at sea  
501 and JMB performed laboratory analysis at the University of Cape Town. JMB analysed the data and prepared  
502 the manuscript with contributions from all co-authors. KEA, MGH and EJ assisted with reviewing and editing  
503 the manuscript.



504 **Competing interests.** One author is a member of the editorial board of journal ACP. The authors declare no  
 505 other conflicts of interest.

506 **Data availability.** Datasets for this research are available at <https://doi.org/10.5281/zenodo.7142722>

507 **Acknowledgements.** We thank the Captain and crew of the R/V *SA Agulhas II* for their support at sea and the  
 508 Marine Biogeochemistry Laboratory in the Oceanography Department at the University of Cape Town for their  
 509 assistance in the field and in the Laboratory. We thank Ruby Ho for analytical support. We thank Riesna Audh,  
 510 Raquel Flynn, Shantelle Smith, Eleonora Puccinelli, Sina Wallschuss, Eesaa Harris and Sive Xokashe for nitrite  
 511 concentration measurements and Sarah Fawcett and Raquel Flynn for quality controlling the nitrite  
 512 concentration data. We thank the South African Weather Service (SAWS) for atmospheric temperature, sea  
 513 level pressure and relative humidity data during all three voyages. This project has received funding from the  
 514 European Union's Horizon 2020 research and innovation programme under grant agreement No 101003826 via  
 515 project CRiceS (Climate Relevant interactions and feedbacks: the key role of sea ice and Snow in the polar and  
 516 global climate system).

517 **Financial Support.** This research has been supported by the South African National Research Foundation  
 518 through a Competitive Support for Rated Researchers Grant to KEA (111716) and a South African National  
 519 Antarctic Programme Postgraduate Fellowship to JMB and Grant to KEA (110732). This research was further  
 520 supported by the University of Cape Town through a University Research Council Launching Grant and VC  
 521 Future Leaders 2030 Grant awarded to KEA. Additional support was provided by the National Research  
 522 Foundation through a doctoral scholarship to JMB (138813) as well as by the European Union's Horizon 2020  
 523 research and innovation programme (Grant agreement No 101003826) via project CRiceS. This work was  
 524 partially supported by the NSF (Award Number: 1851343) via the North Pacific Atmosphere project grant  
 525 awarded to MGH.

## 526 References

- 527 Alexander, B., Sherwen, T., Holmes, C. D., Fisher, J. A., Chen, Q., Evans, M. J., and Kasibhatla, P.: Global  
 528 inorganic nitrate production mechanisms: comparison of a global model with nitrate isotope  
 529 observations, *Atmos. Chem. Phys.*, 20, 3859–3877, <https://doi.org/10.5194/acp-20-3859-2020>, 2020.
- 530 Altieri, K. E., Hastings, M. G., Gobel, A. R., Peters, A. J., and Sigman, D. M.: Isotopic composition of rainwater  
 531 nitrate at Bermuda: the influence of air mass source and chemistry in the marine boundary layer, *J.*  
 532 *Geophys. Res.-Atmos.*, 118, 11304–11316, <https://doi.org/10.1002/jgrd.50829>, 2013.
- 533 Altieri, K. E., Fawcett, S. E., and Hastings, M. G.: Reactive Nitrogen Cycling in the Atmosphere and Ocean,  
 534 *Annu. Rev. Earth Pl. Sc.*, 49, 513–540, <https://doi.org/10.1146/annurev-earth-083120-052147>, 2021.
- 535 Baker, A.R., Weston, K., Kelly, S. D., Voss, M., Streu, P., and Cape, J. N.: Dry and wet deposition of nutrients  
 536 from the tropical Atlantic atmosphere: links to primary productivity and nitrogen fixation, *Deep Sea*  
 537 *Res. Part I Oceanogr. Res. Pap.*, 54(10), 1704–1720, <https://doi.org/10.1016/j.dsr.2007.07.001>, 2007.
- 538 Barkan, E., and Luz, B.: High precision measurements of  $^{17}\text{O}/^{16}\text{O}$  and  $^{18}\text{O}/^{16}\text{O}$  ratios in  $\text{H}_2\text{O}$ , *Rapid Commun.*  
 539 *Mass Spectrom.*, 19, 3737–3742, <https://doi.org/10.1002/rcm.2250>, 2005.
- 540 Berhanu, T. A., Meusinger, C., Erbland, J., Jost, R., Bhattacharya, S. K., Johnson, M. S., and Savarino, J.:  
 541 Laboratory study of nitrate photolysis in Antarctic snow. II. Isotopic effects and wavelength  
 542 dependence, *J. Chem. Phys.*, 140, 244306, <https://doi.org/10.1063/1.4882899>, 2014.



- 543 Berhanu, T. A., Savarino, J., Bhattacharya, S. K., and Vicars, W. C.:  $^{17}\text{O}$  excess transfer during the  $\text{NO}_2 +$   
 544  $\text{O}_3 \rightarrow \text{NO}_3 + \text{O}_2$  reaction, *J. Chem. Phys.*, 136, 1-9, <https://doi.org/10.1063/1.3666852>, 2012.
- 545 Berhanu, T. A., Savarino, J., Erbland, J., Vicars, W. C., Preunkert, S., Martins, J. F., and Johnson, M. S.:  
 546 Isotopic effects of nitrate photochemistry in snow: a field study at Dome C, Antarctica, *Atmos. Chem.*  
 547 *Phys.*, 15, 11243–11256, <https://doi.org/10.5194/acp-15-11243-2015>, 2015.
- 548 Beygi, Z. H., Fischer, H., Harder, H. D., Martinez, M., Sander, R., Williams, J., Brookes, D. M., Monks, P. S.,  
 549 and Lelieveld, J.: Oxidation photochemistry in the Southern Atlantic boundary layer: unexpected  
 550 deviations of photochemical steady state, *Atmos. Chem. Phys.*, 11, 8497–8513,  
 551 <https://doi.org/10.5194/acp-11-8497-2011>, 2011.
- 552 Böhlke, J. K., Mroczkowski, S. J., and Coplen, T. B.: Oxygen isotopes in nitrate: new reference materials for  
 553  $^{18}\text{O}$ : $^{17}\text{O}$ : $^{16}\text{O}$  measurements and observations on nitrate-water equilibrium, *Rapid Commun. Mass Sp.*,  
 554 17, 1835–1846, <https://doi.org/10.1002/rcm.1123>, 2003.
- 555 Brough, N., Jones, A. E., and Griffiths, P. T.: Influence of sea ice derived halogens on atmospheric HOx as  
 556 observed in Springtime coastal Antarctica, *Geophys. Res. Lett.*, 46, 10168–10176,  
 557 <https://doi.org/10.1029/2019GL083825>, 2019.
- 558 Burger, J. M., Granger, J., Joyce, E., Hastings, M. G., Spence, K. A. M., and Altieri, K. E.: The importance of  
 559 alkyl nitrates and sea ice emissions to atmospheric NOx sources and cycling in the summertime  
 560 Southern Ocean marine boundary layer, *Atmos. Chem. Phys.*, 22, 1081–1096,  
 561 <https://doi.org/10.5194/acp-22-1081-2022>, 2022.
- 562 Casciotti, K. L., Sigman, D. M., Hastings, M. G., Böhlke, J. K., and Hilkert, A.: Measurement of the oxygen  
 563 isotopic composition of nitrate in seawater and freshwater using the denitrifier method, *Anal. Chem.*,  
 564 74, 4905–4912, <https://doi.org/10.1021/ac020113w>, 2002.
- 565 Dahl, E. E. and Saltzman, S. E.: Alkyl nitrate photochemical production rates in North Pacific seawater, *Mar.*  
 566 *Chem.*, 112, 137–141, <https://doi.org/10.1016/j.marchem.2008.10.002>, 2008.
- 567 Dahl, E. E., Heiss, E. M., and Murawski, K.: The effects of dissolved organic matter on alkyl nitrate production  
 568 during GOMECC and laboratory studies, *Mar. Chem.*, 142, 11–17,  
 569 <https://doi.org/10.1016/j.marchem.2012.08.001>, 2012.
- 570 Dar, S. S., Ghosh, P., Swaraj, A., and Kumar, A.: Graig-Gordon model validation using observed  
 571 meteorological parameters and measured stable isotope ratios in water vapor over the Southern Ocean,  
 572 *Atmos. Chem. Phys.*, 20, 11435–11449, <https://doi.org/10.5194/acp-20-11435-2020>, 2020.
- 573 Davidson, E. A. and Kingerlee, W.: A global inventory of nitric oxide emissions from soils, *Nutr. Cycl.*  
 574 *Agroecosys.*, 48, 37–50, <https://doi.org/10.1023/A:1009738715891>, 1997.
- 575 Derwent, R. G., Parrish, D. D., Galbally, I. E., Stevenson, D. S., Doherty, R. M., Young, P. J., and Shallcross,  
 576 D. E.: Interhemispheric differences in seasonal cycles of tropospheric ozone in the marine boundary  
 577 layer: Observation-model comparisons, *J. Geophys. Res. Atmos.*, 121, 11075–11085,  
 578 <https://doi.org/10.1002/2016JD024836>, 2016.
- 579 Elliott, E. M., Kendall, C., Wankel, S. D., Burns, S. A., Boyer, E. W., Harlin, K., Bain, D. J., and Butler, T. J.:  
 580 Nitrogen isotopes as indicators of NOx source contributions to atmospheric nitrate deposition across  
 581 the Midwestern and Northeastern United States, *Environ. Sci. Technol.*, 41, 7661–7667,  
 582 <https://doi.org/10.1021/es070898t>, 2007.





- 583 Elliot, E. M., Yu, Z., Cole, A. S., and Coughlin, J. G.: Isotopic advances in understanding reactive nitrogen  
 584 deposition and atmospheric processing, *Sci. Total Environ.*, 662, 393-403,  
 585 <https://doi.org/10.1016/j.scitotenv.2018.12.177>, 2019.
- 586 Fang, Y. T., Koba, K., Wang, X. M., Wen, D. Z., Li, J., Takebayashi, Y., Liu, X. Y., and Yoh, M.:  
 587 Anthropogenic imprints on nitrogen and oxygen isotopic composition of precipitation nitrate in a  
 588 nitrogen-polluted city in southern China, *Atmos. Chem. Phys.*, 11, 1313-1325,  
 589 <https://doi.org/10.5194/acp-11-1313-2011>, 2011.
- 590 Fibiger, D. L., Hastings, M. G., Dibb, J. E., and Huey, L. G.: The preservation of atmospheric nitrate in snow at  
 591 Summit, Greenland, *Geophys. Res. Lett.*, 40, 3484-3489, <https://doi.org/10.1002/grl.50659>, 2013.
- 592 Finlayson-Pitts, B. J. and Pitts, J. N.: *Chemistry of the upper and lower troposphere*, Academic Press, San  
 593 Diego, California, <https://doi.org/10.1016/B978-0-12-257060-5.X5000-X>, 2000.
- 594 Fisher, J. A., Atlas, E. L., Barletta, B., Meinardi, S., Blake, D. R., Thompson, C. R., Ryerson, T. B., Peischl, J.,  
 595 Tzompa-Sosa, Z. A., and Murray, L. T.: Methyl, ethyl and propyl nitrates: global distribution and  
 596 impacts on reactive nitrogen in remote marine environments, *J. Geophys. Res.-Atmos.*, 123, 12412–  
 597 12429, <https://doi.org/10.1029/2018JD029046>, 2018.
- 598 Frey, M. M., Savarino, J., Morin, S., Erbland, J., and Martins, J. M. F.: Photolysis imprint in the nitrate stable  
 599 isotope signal in snow and atmosphere of East Antarctica and implications for reactive nitrogen  
 600 cycling, *Atmos. Chem. Phys.*, 9, 8681–8696, <https://doi.org/10.5194/acp-9-8681-2009>, 2009.
- 601 Grasshoff, K., Kremling, K., and Ehrhardt, M.: *Methods of seawater analysis*, Verlag Chemi, Florida, 1983.
- 602 Hamilton, D. S., Lee, L. A., Pringle, K. J., Reddington, C. L., Spracklen, D. V., and Carslaw, K. S.: Occurrence  
 603 of pristine aerosol environments on a polluted planet, *P. Natl. Acad. Sci. USA*, 111, 18466–18471,  
 604 <https://doi.org/10.1073/pnas.1415440111>, 2014.
- 605 Hastings, M. G., Sigman, D. M., and Lipschultz, F.: Isotopic evidence for source changes of nitrate in rain at  
 606 Bermuda, *J. Geophys. Res.*, 108, 4790, <https://doi.org/10.1029/2003JD003789>, 2003.
- 607 Haywood, J. and Boucher, O.: Estimates of the direct and indirect radiative forcing due to tropospheric aerosols:  
 608 a review, *Rev. Geophys.*, 38, 513–543, <https://doi.org/10.1029/1999RG000078>, 2000.
- 609 Hoering, T.: The isotopic composition of the ammonia and the nitrate ion in rain, *Geochim. Cosmochim. Ac.*,  
 610 12, 97–102, [https://doi.org/10.1016/0016-7037\(57\)90021-2](https://doi.org/10.1016/0016-7037(57)90021-2), 1957.
- 611 IPCC: Boucher, O. D., Randall, P., Artaxo, C., Bretherton, G., Feingold, P., Forster, V.-M., Kerminen, Y.,  
 612 Kondo, H., Liao, U., Lohmann, P., Rasch, S.K., Satheesh, S., Sherwood, B., Stevens, and Zhang, X. Y.:  
 613 Clouds and Aerosols, in: *Climate Change 2013: The Physical Science Basis. Contribution of Working*  
 614 *Group I to the Fifth Assessment Report of the Intergovernmental Panel on Climate Change*, edited by:  
 615 Stocker, T. F., Qin, D., Plattner, G.-K., Tignor, M., Allen, S. K., Boschung, J., Nauels, A., Xia, Y., Bex,  
 616 V., and Midgley, P. M., Cambridge University Press, Cambridge, United Kingdom and New York,  
 617 NY, USA, 2013.
- 618 Ireland, T. R., Avila, J., Greenwood, R. C., Hicks, L. J., and Bridges, J. C.: Oxygen Isotopes and Sampling of  
 619 the Solar System, *Space Sci. Rev.*, 216(25), 1-60, <https://doi.org/10.1007/s11214-020-0645-3>, 2020.
- 620 Ishino, S., Hattori, S., Savarino, J., Jourdain, B., Preunkert, S., Legrand, M., Caillon, N., Barbero, A.,  
 621 Kuribayashi, K., and Yoshida, N.: Seasonal variations of triple oxygen isotopic compositions of



- 622 atmospheric sulfate, nitrate, and ozone at Dumont d'Urville, coastal Antarctica, *Atmos. Chem. Phys.*,  
 623 17, 3713–3727 <https://doi.org/10.5194/acp-17-3713-2017>, 2017.
- 624 Jacobi, H.-W., Weller, R., Jones, A. E., Anderson, P. S., & Schrems, O.: Peroxyacetyl nitrate (PAN)  
 625 concentrations in the Antarctic troposphere measured during the photochemical experiment at  
 626 Neumayer (PEAN'99), *Atmos. Environ.*, 34, 5235–5247, [https://doi.org/10.1016/S1352-](https://doi.org/10.1016/S1352-2310(00)00190-4)  
 627 2310(00)00190-4, 2000.
- 628 Jones, A. E., Weller, R., Wolff, E. W., and Jacobi, H.-W.: Speciation and rate of photochemical NO and NO<sub>2</sub>  
 629 production in Antarctic snow, *Geophys. Res. Lett.*, 27, 345–348,  
 630 <https://doi.org/10.1029/1999GL010885>, 2000.
- 631 Jones, A. E., Weller, R., Anderson, P. S., Jacobi, H.-W., Wolff, E. W., Schrems, O., and Miller, H.:  
 632 Measurements of NO<sub>x</sub> emissions from the Antarctic snowpack, *Geophys. Res. Lett.*, 28, 1499–1502,  
 633 <https://doi.org/10.1029/2000GL011956>, 2001.
- 634 Joyce, E. E., Balint, S. J., and Hastings, M. G.: Isotopic evidence that alkyl nitrates are important to aerosol  
 635 nitrate formation in the equatorial Pacific, *Geophys. Res. Lett.*, 49(16), 1–10,  
 636 <https://doi.org/10.1029/2022GL099960>, 2022.
- 637 Kaiser, J., Hastings, M. G., Houlton, B. Z., Rockmann, T., and Sigman, D. M.: Triple Oxygen Isotope Analysis  
 638 of Nitrate Using the Denitrifier Method and Thermal Decomposition of N<sub>2</sub>O, *Anal. Chem.*, 79, 599–  
 639 607, <https://doi.org/10.1021/ac061022s>, 2007.
- 640 Kamezaki, K., Hattori, S., Iwamoto, Y., Ishino, S., Furutani, H., Miki, Y., Uematsu, M., Miura, K., and  
 641 Yoshida, N.: Tracing the sources and formation pathways of atmospheric particulate nitrate over the  
 642 Pacific Ocean using stable isotopes, *Atmos. Environ.*, 209, 152–166,  
 643 <https://doi.org/10.1016/j.atmosenv.2019.04.026>, 2019.
- 644 Kasibhatla, P., Sherwen, T., Evans, M. J., Carpenter, L. J., Reed, C., Alexander, B., Chen, Q., Sulprizio, M. P.,  
 645 Lee, J. D., Read, K. A., Bloss, W., Crilley, L. R., Keene, W. C., Pszenny, A. A. P., and Hodzic, A.:  
 646 Global impact of nitrate photolysis in sea-salt aerosol on NO<sub>x</sub>, OH, and O<sub>3</sub> in the marine boundary  
 647 layer, *Atmos. Chem. Phys.*, 18, 11185–11203, <https://doi.org/10.5194/acp-18-11185-2018>, 2018.
- 648 Lakkala, K., Aun, M., Sanchez, R., Bernhard, G., Asmi, E., Meinander, O., Nollas, F., Hülsen, G., Karppinen,  
 649 T., Aaltonen, V., Arola, A., and de Leeuw, G.: New continuous total ozone, UV, VIS and PAR  
 650 measurements at Marambio, 64°S, Antarctica, *Earth Syst. Sci. Data*, 12, 947–960,  
 651 <https://doi.org/10.5194/essd-12-947-2020>, 2020.
- 652 Lawrence, M. G., and Crutzen, P. J.: Influence of NO<sub>x</sub> emissions from ships on tropospheric photochemistry  
 653 and climate, *Nature*, 402, 167–170, <https://doi.org/10.1038/46013>, 1999.
- 654 Lee, H.-M., Henze, D. K., Alexander, B., and Murray, L. T.: Investigating the sensitivity of surface-level nitrate  
 655 seasonality in Antarctica to primary sources using a global model, *Atmos. Environ.*, 89, 757–767,  
 656 <https://doi.org/10.1016/j.atmosenv.2014.03.003>, 2014.
- 657 Li, J., Davy, P., Harvey, M., Katzman, T., Mitchell, T., and Michalski, G.: Nitrogen isotopes in nitrate aerosols  
 658 collected in the remote marine boundary layer: Implications for nitrogen isotopic fractionations among  
 659 atmospheric reactive nitrogen species, *Atmos. Environ.*, 245, 1–10,  
 660 <https://doi.org/10.1016/j.atmosenv.2020.118028>, 2021.



- 661 Li, C., Chen, J., Angot, H., Zheng, W., Shi, G., Ding, M., Du, Z., Zhang, Q., Ma, X., Kang, S., Xiao, C., Ren, J.,  
 662 and Qin, D.: Seasonal Variation of Mercury and its Isotopes in Atmospheric Particles at the Coastal  
 663 Zhongshan Station, Eastern Antarctica, *Environ. Sci. Technol.*, 54, 11344–11355,  
 664 <https://dx.doi.org/10.1021/acs.est.0c04462>, 2020.
- 665 McCabe, J. R., Thiemens, M. H., Savarino, J.: A record of ozone variability in South Pole Antarctic snow: Role  
 666 of nitrate oxygen isotopes, *J. Geophys. Res.*, 112, D12303, <https://doi.org/10.1029/2006JD007822>,  
 667 2007.
- 668 Michalski, G., Scott, Z., Kabling, M., and Thiemens, M. H.: First measurements and modeling of  $\Delta^{17}\text{O}$  in  
 669 atmospheric nitrate, *Geophys. Res. Lett.*, 30, 1870, <https://doi.org/10.1029/2003GL017015>, 2003.
- 670 Michalski, G., and Bhattacharya, S. K.: The role of symmetry in the mass independent isotope effect in ozone,  
 671 *PNAS*, 106(14), 5493–5496, <http://www.jstor.org/stable/40454817>, 2009.
- 672 Michalski, G., Bhattacharya, S. K., and Mase, D. F.: Oxygen isotope dynamics of atmospheric nitrate and its  
 673 precursor molecules, in: *Handbook of environmental isotope geochemistry. Advances in Isotope*  
 674 *Geochemistry*, edited by: Baskaran, M., Springer, Berlin, Heidelberg, 613–635,  
 675 [https://doi.org/10.1007/978-3-642-10637-8\\_30](https://doi.org/10.1007/978-3-642-10637-8_30), 2012.
- 676 Morin, S., Savarino, J., Frey, M. M., Domine, F., Jacobi, H. W., Kaleschke, L., and Martins, J. M.:  
 677 Comprehensive isotopic composition of atmospheric nitrate in the Atlantic Ocean boundary layer from  
 678 65° S to 79° N, *J. Geophys. Res.*, 114, D05303, <https://doi.org/10.1029/2008JD010696>, 2009.
- 679 Morin, S., Sander, R., Savarino, J.: Simulation of the diurnal variations of the oxygen isotope anomaly ( $\Delta^{17}\text{O}$ ) of  
 680 reactive atmospheric species, *Atmos. Chem. Phys.*, 11, 3653–3671, [https://doi.org/10.5194/acp-11-](https://doi.org/10.5194/acp-11-3653-2011)  
 681 3653-2011, 2011.
- 682 Nesbitt, S. W., Zhang, R., and Orville, R. E.: Seasonal and global NO<sub>x</sub> production by lightning estimated from  
 683 the Optical Transient Detector (OTD), *Tellus B*, 52, 1206–1215,  
 684 <https://doi.org/10.3402/tellusb.v52i5.17098>, 2000.
- 685 Obbard, R. W.: Microplastics in Polar Regions: The role of long range transport, *Curr. Opin. in Environ. Sci.*, 1,  
 686 24–29, <https://doi.org/10.1016/j.coesh.2017.10.004>, 2018.
- 687 Park, S. S. and Kim, Y. J.: Source contributions to fine particulate matter in an urban atmosphere, *Chemosphere*,  
 688 59, 217–226, <https://doi.org/10.1016/j.chemosphere.2004.11.001>, 2005.
- 689 Paton-Walsh, C., Emmerson, K. M., Garland, R. M., Keywood, M., Hoelzemann, J. J., Huneus, N., Buchholz,  
 690 R. R., Humphries, R. S., Altieri, K., Schmale, J., Wilson, S. R., Labuschagne, C., Kalisa, E., Fisher, J.  
 691 A., Deutscher, N. M., van Zyl, P. G., Beukes, J. P., Joubert, W., Martin, L., Mkololo, T., Barbosa, C.,  
 692 Anrade, M. de F., Schofield, R., Mallet, M. D., Harvey, M. J., Formenti, P., Piketh, S. J., and Olivares,  
 693 G.: Key challenges for tropospheric chemistry in the Southern Hemisphere, *Elem. Sci. Anth.*, 10(1), 1–  
 694 35, <https://doi.org/10.1525/elementa.2021.00050>, 2022.
- 695 Reed, C., Evans, M. J., Crilley, L. R., Bloss, W. J., Sherwen, T., Read, K. A., Lee, J. D., and Carpenter, L. J.:  
 696 Evidence for renoxification in the tropical marine boundary layer, *Atmos. Chem. Phys.*, 17, 4081–4092,  
 697 <https://doi.org/10.5194/acp-17-4081-2017>, 2017.
- 698 Rolph, G. D.: Real-time Environmental Applications and Display System (READY) Website, NOAA Air  
 699 Resources Laboratory, College Park, MD, available at: <https://www.ready.noaa.gov/index.php> (last  
 700 access: June 2022), 2016.



- 701 Romer, P. S., Wooldridge, P. J., Crounse, J. D., Kim, M. J., Wennberg, P. O., Dibb, J. E., Scheuer, E., Blake, D.  
 702 R., Meinardi, S., Brosius, A. L., Thames, A. B., Miller, D. O., Brune, W. H., Hall, S. R., Ryerson, T.  
 703 B., and Cohen, R. C.: Constraints on Aerosol Nitrate Photolysis as a Potential Source of HONO and  
 704 NO<sub>x</sub>, *Environ. Sci. Technol.*, 52, 13738–13746, <https://doi.org/10.1021/acs.est.8b03861>, 2018.
- 705 Savarino, J., Kaiser, J., Morin, S., Sigman, D. M., and Thiemens, M. H.: Nitrogen and oxygen isotopic  
 706 constraints on the origin of atmospheric nitrate in coastal Antarctica, *Atmos. Chem. Phys.*, 7, 1925–  
 707 1945, <https://doi.org/10.5194/acp-7-1925-2007>, 2007.
- 708 Savarino, J., Vicars, W. C., Legrand, M., Preunkert, S., Jourdain, B., Frey, M. M., Kukui, A., Caillon, N., and  
 709 Roca, J. G.: Oxygen isotope mass balance of atmospheric nitrate at Dome C, East Antarctica, during  
 710 the OPALE campaign, *Atmos. Chem. Phys.*, 16, 2659–2673, <https://doi.org/10.5194/acp-16-2659-2016>,  
 711 2016.
- 712 Schmale, J., Baccarini, A., Thurnherr, I., Henning, S., Efraim, A., Regayre, L., Bolas, C., Hartmann, M., Welti,  
 713 A., Lehtipalo, K., Aemisegger, F., Tatzelt, C., Landwehr, S., Modini, R. L., Tummon, F., Johnson, J.  
 714 S., Harris, N., Schnaiter, M., Toffoli, A., Derkani, M., Bukowiecki, N., Stratmann, F., Dommen, J.,  
 715 Baltensperger, U., Wernli, H., Rosenfeld, D., Gysel-Beer, M., and Carslaw, K. S.: Overview of the  
 716 Antarctic Circumnavigation Expedition: study of preindustrial-like aerosols and their climate effects  
 717 (ACE-SPACE), *Bull. Am. Meteorol. Soc.*, 100(11), 2260–2283, 2019.
- 718 Schumann, U. and Huntrieser, H.: The global lightning-induced nitrogen oxides source, *Atmos. Chem. Phys.*, 7,  
 719 3823–3907, <https://doi.org/10.5194/acp-7-3823-2007>, 2007.
- 720 Shi, G., Buffen, A. M., Ma, H., Hu, Z., Sun, B., Li, C., Yu, J., Ma, T., An, C., Jiang, S., Li, Y., and Hastings, M.  
 721 G.: Distinguishing summertime atmospheric production of nitrate across the East Antarctic ice sheet,  
 722 *Geochim. Cosmochim. Ac.*, 231, 1–14, <https://doi.org/10.1016/j.gca.2018.03.025>, 2018.
- 723 Shi, G., Ma, H., Zhu, Z., Hu, A., Chen, Z., Jiang, Su., An, C., Yu, J., Ma, T., Li, Y., Sun, B., and Hastings, M.  
 724 G.: Using stable isotopes to distinguish atmospheric nitrate production and its contribution to the  
 725 surface ocean across hemispheres, *Earth & Planet. Sci. Lett.*, 564, 116914,  
 726 <https://doi.org/10.1016/j.epsl.2021.116914>, 2021.
- 727 Shi, G., Li, C., Li, Y., Chen, Z., Ging, M., Ma, H., Jiang, S., An, C., Guo, J., Sun, B., and Hastings, M. Q.:  
 728 Isotopic constraints on sources, production, and phase partitioning for nitrate in the atmosphere and  
 729 snowfall in coastal East Antarctica, *Earth & Planet. Sci. Lett.*, 578, 1–12,  
 730 <https://doi.org/10.1016/j.epsl.2021.117300>, 2022.
- 731 Sigman, D. M., Casciotti, K. L., Andreani, M., Barford, C., Galanter, M., and Böhlke, J. K.: A bacterial method  
 732 for the nitrogen isotopic analysis of nitrate in seawater and freshwater, *Anal. Chem.*, 73, 4145–4153,  
 733 <https://doi.org/10.1021/ac010088e>, 2001.
- 734 Stein, A. F., Draxler, R. R., Rolph, G. D., Stunder, B. J. B., Cohen, M. D., and Ngan, F.: NOAA's HYSPLIT  
 735 atmospheric transport and dispersion modeling system, *B. Am. Meteorol. Soc.*, 96, 2059–2077,  
 736 <https://doi.org/10.1175/BAMS-D-14-00110.1>, 2015.
- 737 Thiemens, M. H.: History and Applications of Mass-Independent Isotope Effects, *Annu. Rev. Earth Planet. Sci.*,  
 738 34, 217–262, <https://doi.org/10.1146/annurev.earth.34.031405.125026>, 2006.
- 739 van der A, R. J., Eskes, H. J., Boersma, K. F., van Noije, T. P., Van Roozendael, M., De Smedt, I., Peters, D. H.  
 740 M. U., and Meijer, E. W.: Trends, seasonal variability and dominant NO<sub>x</sub> source derived from a ten



- 741 year record of NO<sub>2</sub> measured from space, *J. Geophys. Res.*, 113, D04302,  
 742 <https://doi.org/10.1029/2007JD009021>, 2008.
- 743 Vicars, W. C. and Savarino, J.: Quantitative constraints on the 17O-excess (17O) signature of surface ozone:  
 744 Ambient measurements from 50° N to 50° S using the nitrite-coated filter technique, *Geochim.*  
 745 *Cosmochim. Ac.*, 135, 270–287, <https://doi.org/10.1016/j.gca.2014.03.023>, 2014.
- 746 Von Savigny, C., Ulasi, E.P., Eichmann, K.-U., Bovensmann, H., and Burrows, J. P.: Detection and mapping of  
 747 polar stratospheric clouds using limb scattering observations, *Atmos. Chem. Phys.*, 5, 3071–3079,  
 748 <https://doi.org/10.5194/acp-5-3071-2005>, 2005.
- 749 Wagenbach, D., Legrand, M., Fischer, H., Pichlmayer, F., and Wolff, E.W.: Atmospheric near-surface nitrate at  
 750 coastal Antarctic sites, *J. Geophys. Res.*, 103(D9), 11007–11020, <https://doi.org/10.1029/97JD03364>,  
 751 1998.
- 752 Walters, W. W. and Michalski, G.: Theoretical calculation of nitrogen isotope equilibrium exchange  
 753 fractionation factors for various NO<sub>y</sub> molecules, *Geochim. Cosmochim. Ac.*, 164, 284–297,  
 754 <https://doi.org/10.1016/j.gca.2015.05.029>, 2015.
- 755 Walters, W. W., Simonini, D. S., and Michalski, G.: Nitrogen isotope exchange between NO and NO<sub>2</sub> and its  
 756 implications for δ<sup>15</sup>N variations in tropospheric NO<sub>x</sub> and atmospheric nitrate, *Geophys. Res. Lett.*, 43,  
 757 440–448, <https://doi.org/10.1002/2015GL066438>, 2016.
- 758 Walters, W. W., Michalski, G., Bohlke, J. K., Alexander, B., Savarino, J., and Thiemens, M. H.: Assessing the  
 759 seasonal dynamic of nitrate and sulfate aerosols at the South Pole utilizing stable isotopes, *J. Geophys.*  
 760 *Res.-Atmos.*, 124, 8161–8177, <https://doi.org/10.1029/2019JD030517>, 2019.
- 761 Wang, Z., Stephens, G., Deshler, T., Trepre, C., Parish, T., Vane, D., Winker, D., Liu, D., and Adhikari, L.:  
 762 Association of Antarctic polar stratospheric cloud formation on tropospheric cloud systems, *Geophys.*  
 763 *Res. Lett.*, 35, L13806, <https://doi.org/10.1029/2008GL034209>, 2008.
- 764 Winton, V. H. L., Ming, A., Caillon, N., Hauge, L., Jones, A. E., Savarino, J., Yang, X., and Frey, M. M.:  
 765 Deposition, recycling, and archival of nitrate stable isotopes between the air-snow interface:  
 766 comparison between Dronning Maud Land and Dome C, Antarctica, *Atmos. Chem. Phys.*, 20, 5861–  
 767 5885, <https://doi.org/10.5194/acp-20-5861-2020>, 2020.
- 768 Ye, C., Zhou, X., Pu, D., Stutz, J., Festa, J., Spolaor, M., Tsai, C., Cantrell, C., Mauldin III, R. L., Campos, T.,  
 769 Weinheimer, A., Hornbrook, R. S., Apel, E. C., Guenther, A., Kaser, L., Yuan, B., Karl, T., Haggerty,  
 770 J., Hall, S., Ullmann, K., Smith, J. N., Ortega, J., and Christoph, K.: Rapid cycling of reactive nitrogen  
 771 in the marine boundary layer, *Nature*, 532, 489–491, <https://doi.org/10.1038/nature17195>, 2016.
- 772 Zhou, X., Gao, H., He, Y., Huang, G., Bertman, S. B., Civerolo, K., and Schwab, J.: Nitric acid photolysis on  
 773 surfaces in low-NO<sub>x</sub> environments: Significant atmospheric implications, *Geophys. Res. Lett.*, 23,  
 774 2217, <https://doi.org/10.1029/2003GL018620>, 2003.
- 775 Zong, Z., Wang, X., Tian, C., Chen, Y., Fang, Y., Zhang, F., Li, C., Sun, J., Li, J., and Zhang, G.: First  
 776 assessment of NO<sub>x</sub> sources at a regional background site in North China using isotopic analysis linked  
 777 with modeling, *Environ. Sci. Technol.*, 51, 5923–5931, <https://doi.org/10.1021/acs.est.6b06316>, 2017.
- 778